ELECTRONIC STRUCTURE ENGINEERING OF GROUP IV CRYSTALS FOR OPTOELECTRONIC APPLICATIONS – FIRST PRINCIPLES STUDY

by

NORBERT JANIK

(Wrocław University of Science and Technology)

A THESIS SUBMITTED FOR THE DEGREE OF

DOCTOR OF PHILOSOPHY

in

PHYSICAL SCIENCES

in the

FACULTY OF FUNDAMENTAL PROBLEMS OF TECHNOLOGY

of the

WROCŁAW UNIVERSITY OF SCIENCE AND TECHNOLOGY

2021

Supervisor:

dr hab. inż.
Paweł Scharoch

For Caroline... for everything she is

Acknowledgments

I want to thank my supervisor, dr hab. inż. Paweł Scharoch, for all this fruitful years of collaboration. The knowledge passed on by my Tutor and Mentor changed my view of the world. Thank you for the time devoted to me, discussions, joint struggle over the problems posed and openness to every idea. Without you this work would have never been created.

I also want to thank all the people I had the pleasure to cooperate with, dr Maciej P.Polak, prof. dr hab. inż. Robert Kudrawiec, mgr inż. Jakub Ziembicki, mgr inż. Tomasz Woźniak. They showed me the way when I couldn't find it.

For direct thanks also deserve all of my friends from the faculty, most notably, room 503 comrades on this scientific battlefield. Some of them already after graduation. The time spent together, the problems we solved in hours–long discussions, the chats we had during lunches and tips you've been giving me, I cannot prize enough. All of that has shaped a lot the way I am right now.

Thanks are also to all those not mentioned who supported me throughout all the years of my studies and encouraged me to fulfill my dreams.

Contents

Abstract

Electronic structure engineering of group IV crystals for optoelectronic applications – first principles study

by

Norbert Janik

Wrocław University of Science and Technology

This dissertation concerns the theoretical studies of the influence of different types of band structure engineering on electronic properties of group IV semiconducting materials. The aim is to find such systems that allow for optoelectronics applications.

Four methods to manipulate the parameters of the material were presented along with step by step procedure how to achieve and process the results of calculations to acquire necessary properties. For some specifications more detailed explanation was needed, due to difficulties in interpretation or the way of conducting the calculations. In case of each method: strains, alloying, structural changes and spacial confinement, the most important physical effects are shown along with the explanation of the mechanism. Also in the materials where the electronic properties allow to use in optoelectronics systems, the most important parameters for applications, e.g. electrons and holes mobility, are estimated.

In addition to presenting results and their analysis, the dissertation contains expanded theoretical introduction, related to all discussed problems. Also some useful derivations and proofs can be found in the Appendix attached to the thesis.

Streszczenie

Inżynieria struktury elektronowej kryształów z grupy IV do zastosowań w optoelektronice – obliczenia *ab initio*

Norbert Janik

Politechnika Wrocławska

Niniejsza rozprawa dotyczy teoretycznych badań wpływu różnych typów inżynierii struktury elektronowej na elektronowe własności materiałów półprzewodnikowych z grupy IV. Celem rozprawy jest znalezienie takich układów, które pozwolą na zastosowanie w optoelektronice.

Cztery metody wpływu na własności materiałów zostały zaprezentowane wraz z opisem jak krok po kroku przeprowadzać obliczenia, aby uzyskać porządane wyniki. W przypadku niektórych etapów obliczeń konieczne były szczegółowe wyjaśnienia ze względu na trudności związane z interpretacją lub sposobem przeprowadzania pewnych obliczeń. Dla każdej z wymienionych metod: odkształeń, stopów, zmianyn strukturalnych oraz czynnika przestrzennego, najważniejsze efekty fizyczne zostały pokazane wraz z wyjaśnieniem mechanizmów nimi sterujących. Także, dla materiałów, których własności pozwalają na zastosowanie w optoelektronice, najważniejsze parametry aplikacyjne (jak masy efektywne czy mobilność ładunku) zostały oszacowane.

Dodatkowo do zaprezentowanych wyników wraz z analizą, rozprawa zawiera rozszerzony wstęp teoretyczny powiązany z poruszanymi zagadnieniami. Na koniec, w załączniku znaleźć można użyteczne wyprowadzenia stosowane w pracy.

List of Figures

List of Tables

Chapter 1

Introduction

1.1 Motivation

Semiconductor materials are basics of modern world technology. Their usage is wide and spreads for most of the aspects in human live. Wherever to look, one can find semiconductors put to use. Cell phones, computers, laptops, servers, photovoltaic panels, microcontrolers, etc. Most commonly they are electric circuits and electronic devices, both overtaken by silicon technology. Despite the fact that there are many more suitable, in case of physical and chemical properties, materials for electronic applications, none has dethroned silicon. Although a few of them, e.g. graphene, has been hailed successor of silicon. Until now, no material emerged as a substitute, and for a good reason. Silicon has a very well developed technological process. Czochralski's method enabled mass production of silicon wafers with unparalleled purity and low defects rate. Moreover at low cost. Such attributes still keeps silicon as a base material for electronic devices.

The situation differs a lot in case of optoelectronics which bases on photons as carrier of the information, rather than electrons. Such solution requires different physical properties from material than conventional electronics. Materials from which the devices are to be built must be able to emit and detect light with high efficiency. Because of that silicon, due to indirect fundamental band gap, has no use in this area of technology. Obviously, there are suitable materials to do so but one must remember that optoelectronics is not standalone. It requires connection to conventional electronics. That is where the problem lies. Integrating optoelectronics with electronics is not easy. It involves usage of other type of devices that will convert photonic information to electronic one. This elements are blocky and don't allow onboard integration directly printed into the electric circuit. Moreover, their electronic properties must be very strict. Not only direct fundamental band gap is required but also high carrier mobility due to the fact that photons are a lot faster than the electrons. This implies that the information conversion from photonic to electronic one must be fast enough to not bottleneck the speed of photonic information flow.

The motivation for this work is to expand the capabilities and versatility of silicon technology, by finding new materials. Ones that will be integral with the

silicon technological process and meet the optoelectronic devices requirements. The range of materials suitable for this task is wide. If fact too wide to focus on all of them. That is why a choice of certain group of materials must be made. This work focuses on group IV elements. Main argument is easy integration with silicon technology. Carbon, germanium or tin are isovalent with silicon, which means that they possess the same number of valence electrons. This allows to adapt the technological process used with silicon to them as well. At first glance it might seem that those materials have been already thoroughly investigated and their physical properties are well known. Most of papers that can be found are quite old. Since then technology has improved significantly, allowing us to produce materials of lower dimensionality, higher precision of admixtures or their placement in lattice. This opens new opportunities and a chance to obtain the material composed of group IV elements that will meet optoelectronics requirements. As we know basic group IV materials do not fulfill given expectations. To achieve desirable properties electronic structure engineering must be implemented.

1.2 Band structure engineering

There are mainly 4 ways to make modifications in electronic structure of a material. Those are:

1. strains
2. alloying
3. alternative crystal structures
4. quantum confinement

Strains are relatively easy to implement, e.g. by chemical pressure from lattice mismatch during material growth on different base. Depending on material used and type of stains, it gives different effects on electronic structure of a material. They can be isotropic, planar or axial. Isotropic ones do not change the symmetry of crystal, it extends or shortens the length of lattice vectors, but does not change angles between them. Planar or axial strains usually break symmetry of crystal resulting not only in band gap modifications but may also result in band inversions or band splittings.

Alloying is another way to obtain different properties usually by mixing a few materials or doping one with another. Often, the outcome material's parameters are a mixture of properties of entering components, although rarely the feature we investigate behaves linearly with the doping rate. In many cases the relationship is of a parabolic type, which also may lead to new properties of the alloy. With this method of modifications also symmetry breaks, due to atom substitutions or additions in the lattice. Moreover, in case of low doping rate and break of periodicity of crystal, band tend to blur and new bands may emerge in the process.

Alternative crystal structures are more difficult to apply. This method is basically based on a synthesis of metastable crystal structures, i.e. in a space group which differs from that of stable one. New deposition technologies, like molecular beam epitaxy (MBE) or metal–organic chemical vapor deposition (MOCVD), open such opportunities. Usually the structure is induced by the substrate (e.g. wurtzite structure by the (111) surface of zinc blende crystal). As a result a metastable structure is formed. However, the systems must be thermodynamically stable which does not always happen. Obviously, this should lead to new properties of outcome material, and such effect has already been observed and will be discussed in this work.

Quantum confinement, the last method presented, bases on revealing quantum nature of a subject. That can be achieved in many ways, usually by imposing some additional spacial confinement, like in superstructures (systems of quantum wells). Such situation takes place also nanowires or quantum dots. Any kind of discontinuity small enough to show off quantum effects may lead to enormous changes in electronic structure, e.g. bands can fold straightening the fundamental gap.

All methods presented above have been addressed in this work. The theoretical investigations using the large scale, density functional theory (DFT) based computational studies have been performed.

1.3 Theoretical background

All the computations done in this work have been based on the density functional theory (DFT), whose theoretical foundations have been established in the middle 60s of previous century, by P. Hohenberg, W. Kohn [33] and W. Kohn, L. J. Sham [40]. In practice the investigations into various properties of atomic systems begin with solving self–consistently the Kohn–Sham equations:

$$\left(-\frac{1}{2}\nabla_{\mathbf{r}}^2 + \hat{V}^{KS}(\mathbf{r})\right)\psi_i(\mathbf{r}) = E_i\psi_i(\mathbf{r}), \tag{1.1}$$

where

$$\hat{V}^{KS}(\mathbf{r}) = \hat{V}^{ext}(\mathbf{r}) + \frac{\delta E^H}{\delta n(\mathbf{r})} + \frac{\delta E^{XC}}{\delta n(\mathbf{r})} = \hat{V}^{ext}(\mathbf{r}) + \hat{V}^H(\mathbf{r}) + \hat{V}^{XC}(\mathbf{r}). \tag{1.2}$$

is the so called Kohn–Sham potential, containing 3 contributions: the external potential $\hat{V}^{ext}(\mathbf{r})$, the Hartree potential $\hat{V}^H(\mathbf{r})$ and the exchange–correlation (XC) potential $\hat{V}^{XC}(\mathbf{r})$. As it can be seen in Eq. 1.2, two of the contributions, the Hartree potential and the XC potential are functional derivatives with respect to electron density of respective energies. The Hartree energy is just the Coulomb interaction of electron density with itself $\frac{1}{2}\int\int \frac{n(\mathbf{r})n(\mathbf{r}')}{|\mathbf{r}-\mathbf{r}'|}d\mathbf{r}\,d\mathbf{r}$ and the XC energy is a correction resulting from all the quantum specific interactions (exchange and correlation) in the electronic system. The latter term requires approximations from which the most popular are the local density approximation (LDA) and the general gradient

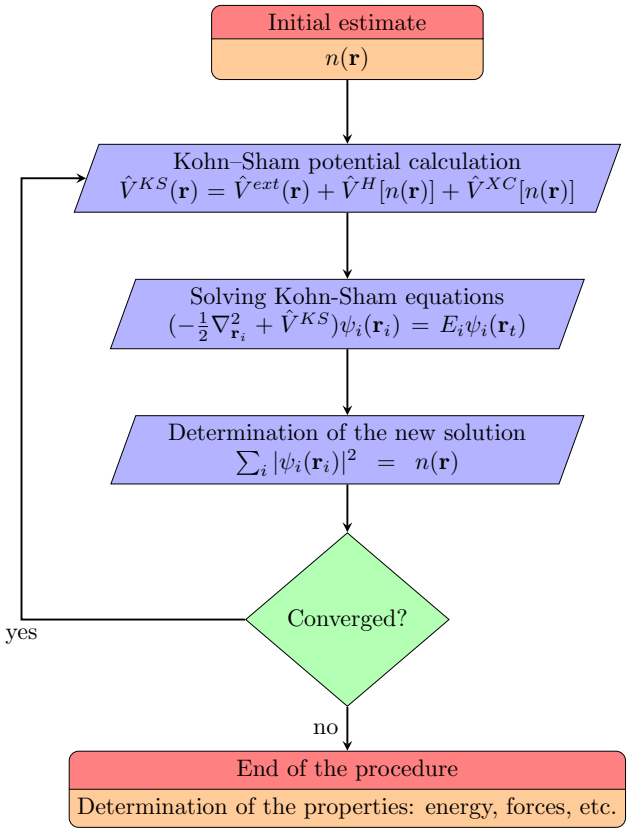

Figure 1.1: Self–consistent procedure of solving Kohn–Sham equations.

approximation (GGA). In fact, constructing various approximations for the XC energy has developed into a separate and, in some extent, independent branch of DFT. One can find a whole gallery of approximations offered by *ab initio* codes, and usually some numerical experiments are the only way to decide which approximation suits best to the system under investigation. This is the most fragile point in the DFT.

It should be noted that all the potentials are local and are the density functionals (except the external one). The electronic density in the theory reads:

$$n(\mathbf{r}) = \sum_{k=occ} |\psi_k(\mathbf{r})|^2 , \tag{1.3}$$

where $\psi_k(\mathbf{r})$ are eigenfunctions of the Kohn–Sham equations (Eq. 1.1) and the summation runs over all the occupied states. Now, the statement above that the Kohn–Sham equations must be solved self–consistently, becomes obvious. This means that starting from some probe density we solve the eigenvalue problem, find new density and repeat the procedure until the total energy is converged (see Fig. 1.1).

In fact the density of an electronic system and its total energy (being a functional of the density, and whose explicit form is known) are the only two physical outputs

of the DFT theory. This seems not too much, but as it will be shown later, many physical properties can be addressed using those two quantities. In that context an interesting fact is that the Kohn–Sham eigenenergies and eigenfunctions in principle have no physical meaning, in particular they can not be treated as the single-particle energies. However, they are often treated as a good first approximation to e.g. electronic band structures in crystals, or form a starting point for the post–DFT methods, like many body perturbation theory (GW). Moreover, in a pure DFT there are some energy functionals which are specially designed to reproduce well the energy bands, among which the most popular are meta–GGA [11] and hybrid functionals.

There are some technical issues which should be also mentioned in this section, these are: representation of the Kohn–Sham equations, representation of atoms and k–space integration.

The Kohn–Sham equations in Eq. 1.1 are given in the position vector representation and in such form are used e.g. in the calculations for atoms. In this case however, the spherical symmetry approximation is exploited which allows to reduce the formula to 1 dimension, and then, as a common practice, a non–uniform grid is used to discretize the equations. In bigger systems like molecules and in particular the periodic systems the position vector representation is not convenient (although also used). In the case of localized systems some localized basis functions are an obvious choice, and one can find here various options (spherical harmonics, gaussians, some specially designed functions etc.). In this thesis periodic systems are dealt with and in this case the plane–wave basis is most suitable. Of course the basis is infinite and must be somehow limited. A convenient way of limiting the basis is to set the maximum kinetic energy which can be reproduced, which is also related to spacial resolution, as in quantum mechanics kinetic energy is proportional to spacial frequency. Thus, the base is limited with the parameter called energy cut–off E_{cut}, and the maximum wave vector in the basis must obey the condition: $\frac{1}{2}G^2 < E_{cut}$ (in Hartree units). The parameter E_{cut} must be subjected to careful convergence study because it is responsible for the quality of the approximation which consists in reducing the solution of the Kohn–Sham equations to certain subspace spanned on a limited basis. The parameter is also responsible for the spacial resolution, i.e. how the fine structure of the wave–functions (e.g. the core atomic regions) will be reproduced. Popular plane–wave codes, Abinit (free) [27, 28] and VASP (comercial) [41, 42] have been used in this work.

Most of atoms have complicated internal electronic structure, which would need a huge plane–wave basis to be well reproduced. However, a good news is that the so called core electrons in atoms have little influence on atomic systems properties, at normal conditions. First, some of them are energetically much below the typical energies of states forming chemical bonds. Second, a part of electrons are localized enough (close to atomic nucleus) to play a role only in the screening of the nuclear charge. Those two facts inspired the development of, in some extent, independent branch of DFT called pseudopotentials and related methods, like very popular projector augmented waves (PAWs) [8, 84]. The latter is the most general approach to representation of atoms, from which all the other approaches can be derived.

As it has been mentions above, the DFT requires the calculation of electronic density given by Eq. 1.3. In principle this is the summation over moduli squared of Kohn–Sham functions but in crystals the functions have the Bloch form and are labelled by 2 indexes: n – an integer assigned to a particular electronic band, and k a wave–vector a (real, continuous numbers). Thus, a summation in Eq. 1.3 must be replaced by the summation over n and integration with respect to k over the Brillouin Zone (BZ). The latter looks difficult since the BZ is a polyhedron. Fortunately, the modulus squared of the Bloch function is periodic both in the r–space and in the k–space. This allows to replace the integration with the summation over certain set of k–points (special k points), which is equivalent to cutting the Fourier series expansion of a periodic function at certain term. The most popular is the Monkhorst–Pack scheme [50], where a regular grid of special k–points is set and then reduced, using crystal symmetry, to irreducible part of BZ. Obviously, the denser is the grid the more accurate is the integration. The number of special k–points used for the BZ integration is an important computational parameter which determines the quality of results and thus must be subjected to careful convergence study.

A detailed description of particular approximations, methods, schemes, used in this work will be given in the following chapters, as they may differ depending on the problem treated.

All the calculations provided here were performed with ABINIT [27, 28, 48] software package or VASP (Vienna Ab initio Symulation Package) [41, 42] (podziękowania centrom obliczeniowym na końcu)

Chapter 2

Strains

In this section the first of the listed in the introduction methods of band structure engineering, the strains, will be addresses. The considerations presented were published in [37].

2.1 Computational method

Applying strains to a material is an easiest way of modifying it's physical properties. In practice many experimental solutions can be found. For example one can apply isotropic (hydrostatic) strains by using diamond anvils or via chemical pressure. The biaxial (planar) strains can be induced by depositing considered material on the surface of another material having different lattice constant (the substrate induced strain). Modern technologies like molecular beam epitaxy (MBE) or metal–organic vapour deposition (MOCVD) provide such opportunities.

In this work three types of strains are considered:

- isotropic (hydrostatic)
- uniaxial (along an axis)
- biaxial (in plane)

In the case of anisotropic strains, crucial is the direction of strain. Different type will usually result in various changes in electronic structure. To have a complete view over the straining effect, in the investigation every meaningful direction must be considered. The choice depends on crystal symmetry and in the case of diamond structure, typical of C, Si, Ge and Sn (α allotrope), relevant directions of strains are [100], [110] and [111]. The directions define both: axial strain (along a direction) and biaxial ones (in plane perpendicular to a direction) denoted as (100), (110) and (111). Other strains can be represented as a linear combination of those. Figure 2.1 shows conventional cell of diamond structure with marked straining directions.

After defining strain types, the range of staining must be set. In the literature many articles can be found, both experimental and theoretical, concerning strains and their effects on electronic properties [36, 52, 77]. Both compressive and tensile strains are investigated, usually in the range of maximum $4 \sim 5\%$ of equilibrium lattice constants, which is dictated by practical reasons and technological limitations.

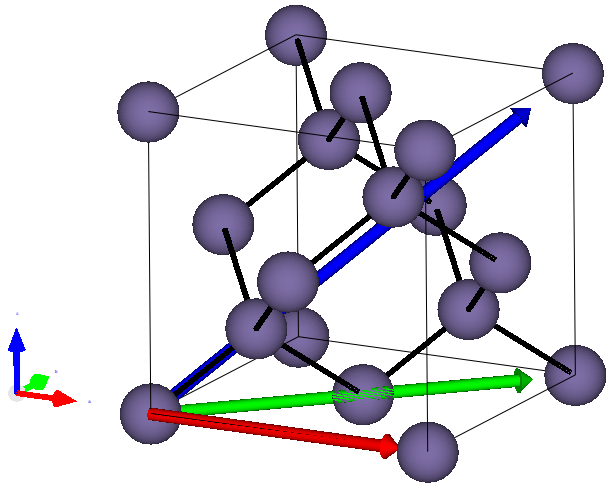

Figure 2.1: Relevant strain directions in the diamond structure: [100], [110], [111].

In this work the range of strains considered is up to 4%. The tensile strains will be represented by positive numbers, while the compressive ones by negative numbers. Although of the main interest was the effect of strain on electronic structure, the investigation began with studying the structural properties, i.e. the effect of strains on lattice parameters and atomic positions.

Thus, the computational procedure was as follows. At first, for every system, a respective elementary cell (supercell) was constructed, which for anisotropic strains differed from the diamond primitive cell (see Figs. 2.2 and 2.3). Then, strains were applied by shortening/elongating respective lattice parameter, the remaining structural degrees of freedom optimized (the other lattice parameters and atomic positions), and induced stresses evaluated.

The supercells lattice vectors a'_1, a'_2 and a'_3 can be related to conventional cell lattice vectors a_1, a_2 and a_3 by transformation matrices, for [100] and [110] strains:

$$\begin{bmatrix} a'_1 \\ a'_2 \\ a'_3 \end{bmatrix} = \begin{bmatrix} 0.5 & 0.5 & 0 \\ -0.5 & 0.5 & 0 \\ 0 & 0 & 1 \end{bmatrix} \begin{bmatrix} a_1 \\ a_2 \\ a_3 \end{bmatrix}, \tag{2.1}$$

and for [111] strains:

$$\begin{bmatrix} a'_1 \\ a'_2 \\ a'_3 \end{bmatrix} = \begin{bmatrix} 0.5 & 0 & 0.5 \\ -0.5 & -0.5 & 0 \\ -1 & 1 & 1 \end{bmatrix} \begin{bmatrix} a_1 \\ a_2 \\ a_3 \end{bmatrix}. \tag{2.2}$$

All the strains were applied in the range between -4% and 4% of the frozen respective lattice parameter and the structures were optimized without imposed symmetries (except identity) to avoid symmetry induced fixing of atomic positions.

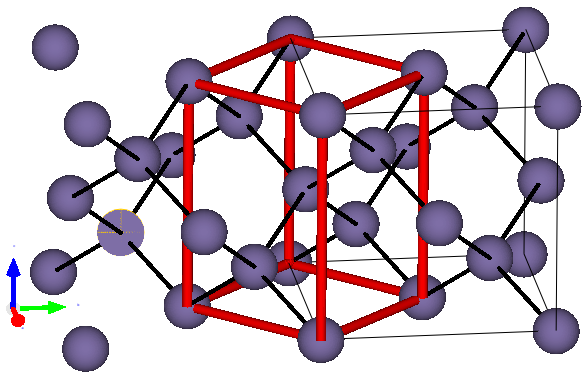

Figure 2.2: Supercell for [100] and [110] strains.

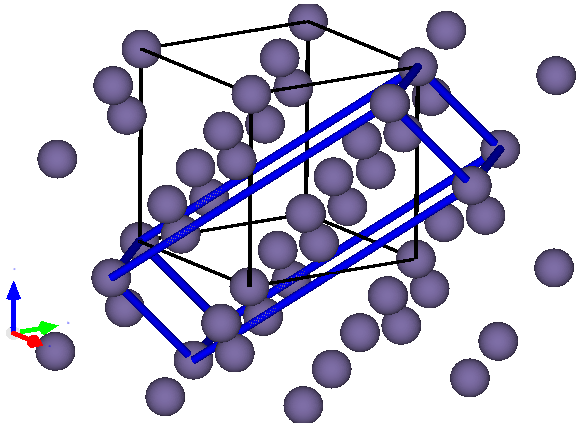

Figure 2.3: Supercell for [111] strains.

2.1.1 Structural and elastic properties

To characterize the structural changes, the Poisson's ratio was used, defined both for the axial and biaxial strains as:

$$\nu = -\frac{\varepsilon_{opt}}{\varepsilon_{ind}}, \tag{2.3}$$

where ε_{ind}, ε_{opt} are respectively an induced and an optimized relative change in the linear dimension along the considered direction and in the plane perpendicular to it. It should be mentioned that the isotropic behavior of a system around chosen axis takes place only for [100] and [111] directions. For [110] Poisson's ratio defined above is not a well established quantity since under axial strain the relative expansion/contraction is not uniform around the axis and is the highest for [001] and the lowest for $[1\bar{1}0]$. Similarly, a uniform strain around [110] axis leads to non–uniform stress. Nevertheless, the [110] direction has also been considered, with the plane degrees of freedom naturally optimized under axial strain and biaxial strain applied uniformly, which may take place if a substrate in epitaxial technology is the (110) surface of a cubic symmetry crystal. It is worth mentioning here that, from the definition, Poisson's ratio is defined for uniaxial strain, and falls within

the range of $0 - 0.5$. To be able to compare results from uniaxial and biaxial strain types, pseudo–Poisson's ratios ware also calculated for biaxially strained systems (later also called Poisson's ratio).

The resulting stresses (σ) appearing at induced strains are described by respective elastic constants, first ($C1$) and second order ($C2$), so that the stress is given by the formula:

$$\sigma = \mathrm{C1} \cdot \varepsilon_{ind} + \mathrm{C2} \cdot \varepsilon_{ind}^2. \tag{2.4}$$

In the above formula ε_{ind} is a fractional relative change (induced) of a given dimension and the constants $C1$ and $C2$ are expressed in GPa. For the case of [110] uniform biaxial strain there are two values of $C1$ and $C2$, corresponding to [001] and $[1\bar{1}0]$ directions. It should be noted that the elastic constants defined above are the standard elastic matrix elements. However, for verification purposes the standard elastic constants have been derived from presented results and compared with the textbook data. In the case of cubic symmetry there are only three non-zero and independent elastic constants (c_{11}, c_{12}, c_{44}). All of them have been calculated from $C1$ and $C2$ values via the specially derived transformation rules.[1]

Because of small differences in results for different strain directions, the average values and standard deviations are given in Tab 2.5.

From the report [30] it is clear that, for realistic structural properties, LDA functional is most suitable for all the four materials studied. The PAW [8, 84] atomic data have been taken as the complementary to LDA, due to resulting realistic forces and stresses.

2.1.2 Electronic structure

In the next step, the electronic structure was studied. The supercell representation of structures is convenient in studying the structural effects of strains but are inconvenient for the band structure analysis, mainly because of the band folding effect which makes it difficult to find meaningful points in the BZ and to identify bands. To avoid this problem, after respective optimization, the representation have been transformed back to BZ–like primitive cell. The detailed derivation of transformation is described in Appendix A. Owing to such an approach the changes in the electronic band structure could have been easily followed since the relative positions of characteristic points in the deformed by strain BZ remained unchanged with respect to the equilibrium state BZ. Of the main focus were characteristic energy gaps between VB and CB, Γ–Γ (direct band gap), Γ – minimum along Δ directions and Γ – minimum along Λ. The expected splittings of energies within Δ and Λ stars caused by an intrinsic for anisotropic strains symmetry breaking can be observed.

As it will be seen in the results some energy gaps exhibit non-smooth behavior with strains, usually when the strain passes through the equilibrium state. To understand better the non–smoothness, the orbital composition of bands have been

[1] Derivation of elastic constants from obtained results can be found in Appendix A

evaluated. This is realized by finding an individual contribution of each orbital of every atom in the system to band energies. Then, the contribution can be traced with straining, which allows to identify the band inversions and band splittings, due to symmetry breaking. This information is sufficient to explain the non smooth behavior of the band gap changes with strains.

In the case of electronic structure calculations, the most prominent choice is mBJLDA [11, 85] approximation for the XC potential [11], which is known for providing realistic band gaps at relatively low computational costs. Characteristic of this potential is the c_TB09 parameter (Eq. 3 in [11]), which in principle is calculated self–consistently but can be also set by hand to adjust the band gap value. In the case of strained systems, where there is a lack of experimental data, the c_TB09 parameter (called her just c) was set as follows

$$\mathrm{c}^{st} = \mathrm{c}^{st}_{sc} \cdot \frac{\mathrm{c}^{eq}_{fit}}{\mathrm{c}^{eq}_{sc}}, \tag{2.5}$$

where *st* means strained, *eq* – equilibrium, *fit* – fit to experiment, *sc* – self-consistent value.

Unfortunately, ABINIT lacks support for PAW atomic data along with mBJLDA, so the HGH [60] pseudopotential has been used instead.

2.1.3 Effective masses and related carriers mobility

Having known the band structures also the effective masses could have been evaluated as functions of strains. The calculations of effective masses were performed by fitting the 3^{rd} order polynomial at bands extrema, which was necessary because of the appearing often asymmetry of bands at these points. For the sake of reliability, 5 to 9 points around band extrema were taken into consideration, and the densities of points along k–space path were subjected to convergence studies. In the CB the effective masses at Γ point as well as at the valleys along Γ-X and Γ-L directions have been calculated, taking into account also the star–degeneracy removal due to the broken symmetry under strain. In the VB only the top of the band at Γ point has been considered, whether it was the heavy or the light hole band (due to inversion of bands). The effective masses were evaluated from the inversion of the second derivative of fitted polynomial at the extremum.

2.1.4 Deformation potentials

The deformations potentials are important characteristics of the semiconductor crystals. They are used e.g. in the band alignment evaluation in semiconductor superstructures or in the calculations of electron–phonon interaction. In this work, the standard deformation potentials a_v, a^{dir}, a^{ind} b, d, Ξ^{Δ}_u, Ξ^{L}_u, as defined in [89] were calculated. In the calculations of a_v, b, and d, which are absolute in the sense that they describe the changes in absolute positions of some points in bands, the crucial point is to establish the unified energy reference point, i.e. the reference point which do not flow with the strain. For that purpose there have been used the

natural slab method [92] in which it is assumed that the energy level in vacuum should not change under strain, and thus defines the energy reference point. There are also a few rules one should keep in mind preparing the calculations:

- for both the slab and the bulk calculations, it is crucial to set the same k–point grid. In a slab a good practice is to adjust the number of k–points to the slab size. E.g. when in bulk the k–points grid is set to $10 \times 10 \times 10$, a corresponding grid for the slab in [100] direction of 5 layers of material and 5–layer–long vacuum is set to $10 \times 10 \times 1$. In that way the slab layer and the bulk have exactly the same k–points distribution.

- vacuum must be long enough for the potential plateau to be clearly visible.

- the flat area should be wide enough for a small potential fluctuations to be averaged, and the vacuum level well established.

Figure 2.4 illustrates where the partial data are taken from in the calculations of a_v in Si under isotropic strain. To establish the unified energy reference point we apply the following assumptions: i) the vacuum level should not change under strain, ii) The rates of the changes in the self–consistent potentials at chosen point in bulk and equivalent point in the slab, under strain, should be the same. Thus, when defining the linear coefficients of lines in Fig. 2.4: a^F – VBM, a^{Vb} – self–consistent potential value at chosen point in bulk (maximum), a^{Vb} – self–consistent potential value at an equivalent point in the slab, a^{Evac} – energy level in vacuum, the deformation potential a_v can be calculated from the formula:

$$a_v = (a^F - a^{Vb} + a^{Vs} - a^{Evac}) \cdot 100/3, \tag{2.6}$$

where the factor 100/3 comes from the transformation from percent to fraction, and from linear to volume change.

The corresponding uncertainties have been calculated from linear coefficients uncertainties in *ab initio* data approximations, assuming the "worst case":

$$\Delta(a_v) = [\Delta(a^F) + \Delta(a^{Vb}) + \Delta(a^{Vs}) + \Delta(a^{Evac})] \cdot 100/3. \tag{2.7}$$

The described procedure was used in the calculations of all the absolute deformation potentials. In the calculation of the relative deformation potentials a^{dir}, Ξ_u^{Δ}, Ξ_u^{L} the above procedure is not necessary because in the energy differences (e.g. $E_c - E_v$) the subtracted energies are always given with respect to the same energy reference point.

Thus, in the calculations the same supercell as for the [100] and [110] structure optimizations have been used except a vacuum layer has been added, i.e. $3 - 4$ layers of optimized supercell and $6 - 7$ supercell–layers–long distance of vacuum. The total potential across the whole supercell (in the direction perpendicular to the slab) was evaluated for slabs with and without separating vacuum layer. As a result the energy variation slopes described above were found, corresponding to respective deformation potentials.

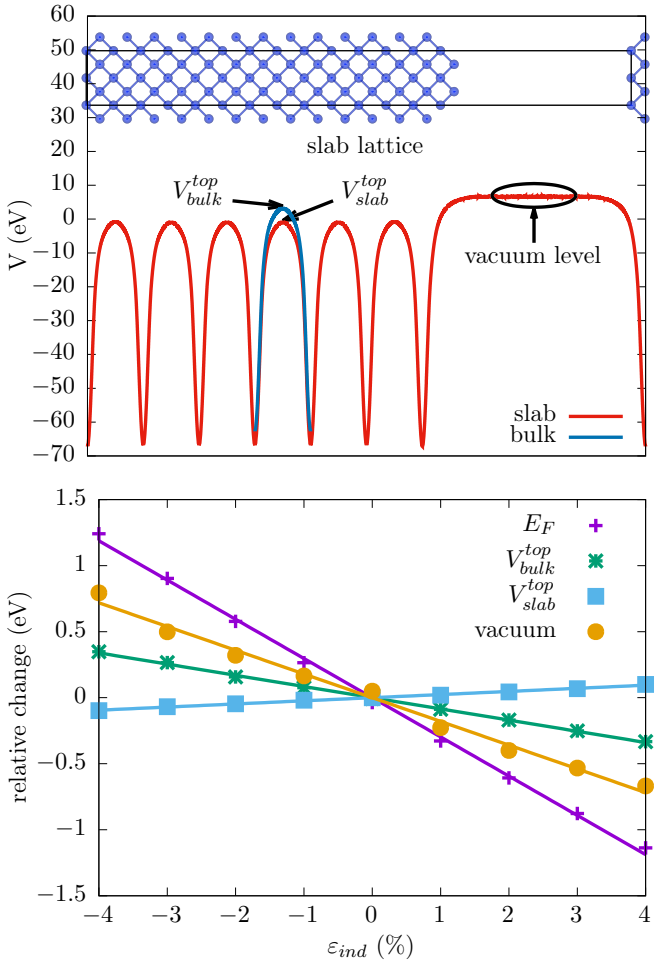

Figure 2.4: Illustration to the deformation potential determination procedure, for Si under isotropic strain. Upper figure: the lattice used and the self–consistent potential throughout this lattice (red line) as well as corresponding potential in bulk (blue line). Lower graph, the strain induced energy variations necessary to evaluate the deformation potential.

2.2 Results

In this section the results of calculations are presented and discussed.

2.2.1 Structural and elastic properties

We begin the discussion of the results from structural and elastic properties of investigated structures, at equilibrium and at applied strains. Table 2.1 shows experimental and calculated (in this work and from the literature) lattice constants. An excellent agreement of calculated values with the experimental ones confirms the appropriate choice of the exchange–correlation functional and PAW data, which also enhances the credibility of other results.

As mentioned previously the strains are applied with respect to [100], [110], and

Table 2.1: Lattice constants (Å).

material	this work	LDA reference [30]	exp. [30]
C	3.530	3.536	3.544
Si	5.402	5.407	5.415
Ge	5.627	5.632	5.639
Sn	6.471	6.481	6.474

[111] directions, axial (along the directions) and biaxial (in the planes perpendicular to the directions). In Fig. 2.5 the strains are shown schematically together with the relations between relative changes in a linear dimension: optimized (ε_{opt}) and corresponding induced change (ε_{ind}).

As explained in the previous chapter, in the case of [110] direction and for the axial strain only the maximum value of the ε_{opt} is shown, i.e. at [100]. The corresponding Poisson's ratios are listed in Tab. 2.2.

Table 2.2: Poisson's ratios (ν) for axial (type 1) and biaxial (type 2) strains.

material	100		110			111	
	1	2	1		2	1	2
C	0.12	0.27	0.13	0.01	0.15	0.05	0.11
Si	0.29	0.81	0.38	0.07	0.55	0.19	0.46
Ge	0.29	0.77	0.38	0.03	0.48	0.17	0.40
Sn	0.34	1.00	0.49	0.04	0.66	0.22	0.57

Some interesting features of the optimized structures can be observed:

1. the induced changes under axial strain are in all the cases significantly smaller than under biaxial strain, with the biggest difference in Sn [100] (0.34 vs 1.00),

2. generally the Poisson's ratios increase from C to Sn, except for Si and Ge where in most cases a sudden drop (between Si and Ge) in the values is observed,

3. the highest value of $\nu = 1$ is for Sn [100] biaxial (which means that the released lattice parameter changes as much as the fixed one),

4. the smallest one $\nu = 0.01$ for C [110] axial (which means that the released lattice parameter almost does not change when the fixed one is varied.

Thus the ν varies in a large range of values (from 0.01 to 1.00) and no systematic behavior can be found (except for features mentioned above).

The strains lead to symmetry breaking which is characterized in Tab. 2.3. In the table one can find the numbers of space groups of equilibrium and strained diamond–like lattices, as well as the names and multiplicity of chosen high symmetry points in the BZ. As it can be seen, in six cases the star–degenerate energies in equilibrium X and L points split into two classes, which is also reflected in the energy gaps graphs which may behave quite differently for split points.

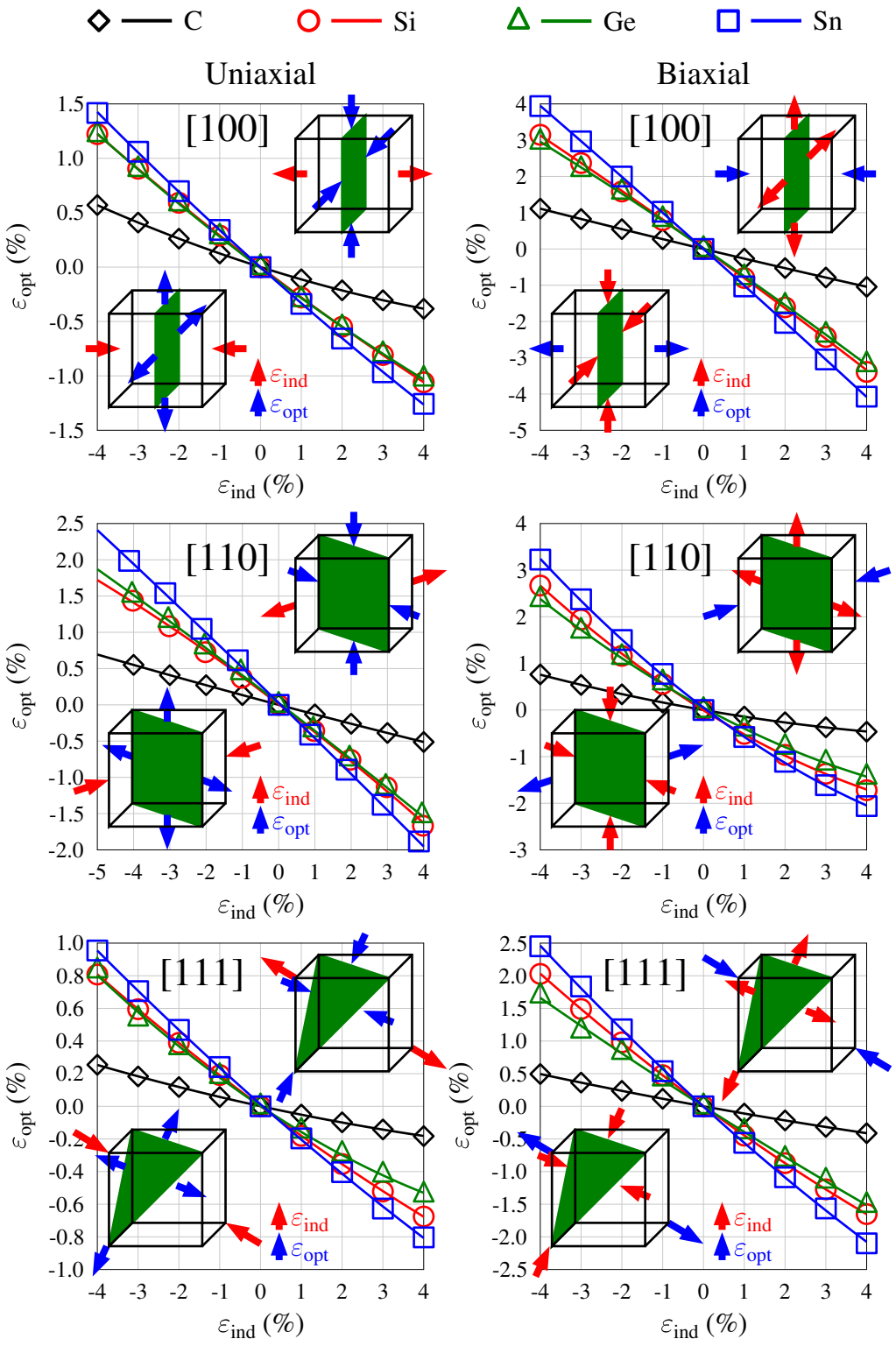

Figure 2.5: Relative changes in linear dimensions, optimized (ε_{opt}) vs.induced (ε_{ind}), for axial strains (left panels) and biaxial strains (right panels).

Table 2.3: Space groups changes of characteristic BZ points in strained diamond type lattice (numbers in parentheses denote the multiplicity of a given point).

	equil.	100	110	111
space group #	227	141	74	166
special points	Γ	Γ	Γ	Γ
	X(6)	X(4)/M(2)	X(2)/R(4)	FB(6)
	L(8)	N(8)	T(4)/S(4)	L(6)/T(2)

To provide a better comprehension of the changes the BZ for each occurring space groups are visualized in Fig. 2.6.

The applied strains, on the one hand, lead to changes of the released degrees of freedom but on the other they induces stresses, as a response of the system. For axial strain for a given axis the stress appears on the plain perpendicular to the axis, whereas for biaxial strain the stress appears on the plains parallel to the axis. The axial symmetry exists except for [110] direction and biaxial uniform strain, where there is a maximum value of the stress at (100) plane and minimum one at (110) plane. The relationship between stress and strain is represented by the first (C1) and the second order (C2) elastic constants in the quadratic function approximation. The elastic constants described above are presented in Tab. 2.4. Here, the chemical trend is clear: the bigger is the atomic number of the element the smaller is the elastic constant. The biggest value of the linear constant C1 is for C at isotropic strain (14.4 GPa), and the smallest one for Sn [100] axial strains (0.45 GPa). As for the second order coefficients, which account for the bowing of the stress vs strain curve, the biggest value is again for C isotropically strained (-0.85 GPa) and the smallest one for Sn biaxially strained with respect to [110] axis (-0.0014 GPa). The negative values of C2 correspond to concave behavior. It is easy to note that at considered strains the resulted strain do not exceed 100 GPa (in diamond) and a few GPa in Sn.

Table 2.4: First (C1) and second order (C2) elastic constants defined in this work (GPa). The 'a' stands for axial, while, 'b' for biaxial.

	param.	100 b	100 a	110 b		110 a	111 b	111 a	isotropic
C	C1	1230	1070	1240	1380	1210	1340	1250	1440
	C2	-4480	-624	-3910	-6410	-3670	-6020	-3730	-8480
Si	C1	175	124	185	227	162	223	180	298
	C2	-595	-224	-99	-444	-385	-722	-88	-2050
Ge	C1	133	93.9	142	180	128	172	143	223
	C2	-610	-205	-145	-538	-362	-884	-19	-1680
Sn	C1	68.3	44.6	76.4	101	64.9	96.6	74.3	141
	C2	-292	-143	-26	-1880	-116	-442	-81	-1100

For verification purposes, the standard elastic constants (for linear regime) have

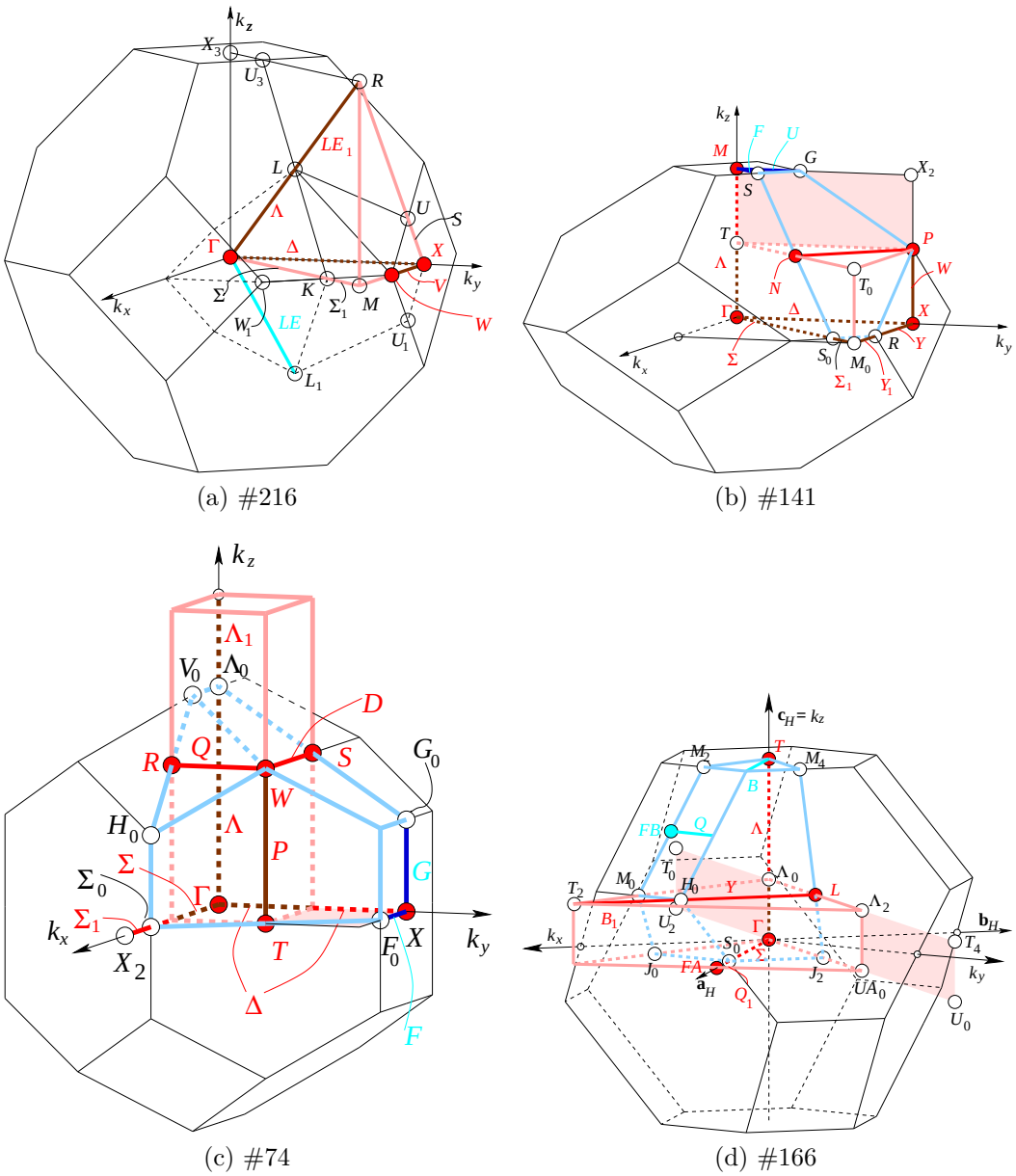

(a) #216 (b) #141

(c) #74 (d) #166

Figure 2.6: Brillouin Zones of strained systems.

been evaluated from our $C1$ and $C2$ constants. The results are presented in Tab. 2.5 and show satisfactory agreement with the textbook data [56].

Table 2.5: Standard elastic constants (GPa) evaluated from data presented in Tab. 2.4 and their comparison with the textbook values[56].

	C	Si	Ge	Sn
calc. c_{11}	1100 ±50	160 ±20	120 ±25	66 ±9
exp. c_{11}	1079	166	126	73.3
calc. c_{12}	160 ±30	70 ±6	52 ±7	50 ±4
exp. c_{12}	124	64	44	67.7
calc. c_{44}	490 ±40	62 ±8	59 ±4	23 ±10
exp. c_{44}	578	79.6	67.7	2.19

2.2.2 Band structures

The evolution of the electronic band structures with applied strains have been represented by changes in the energy differences between the VB maxima and and CB minima at Γ point (direct band gaps) and between the VB maxima and conduction band minima along high symmetry directions Δ and Λ (indirect band gaps). This choice is justified by the fact that the density of states extrema are present at these points and the direct and indirect optical transitions, observed in various spectroscopy experiment take place. The rule of the band gaps presentation, for Ge isotropically strained, is shown in Fig. 2.7. For completeness we also present the evolution of the LH–HH band splitting (Tab. 2.6).

Table 2.6: Linear coefficients for LH–HH bands splitting as function of strain (eV/%).

strain	C	Si	Ge	Sn
100 biaxial	-0.22	-0.14	-0.11	-0.09
100 axial	0.19	0.09	0.08	0.06
110 biaxial	0.11	0.11	0.06	0.06
110 axial	-0.10	-0.11	-0.06	-0.06
111 biaxial	-0.04	-0.11	-0.04	-0.05
111 axial	0.02	0.07	0.05	0.04

The analysis begins from the discussion of typical qualitative behavior of bands which is shown in Fig. 2.8. The orbital character visualization has been used, i.e. the dots of varying color represent a contribution of atomic orbitals to a wave function corresponding to a particular point on the energy diagram (for details see the figure caption), i.e. the color stands for the kind of atomic orbital (spherical harmonics, $s, p, d, ...$) and the intensity for the relative contribution. Two cases are presented there: isotropically strained Sn, whose behavior is similar to that of Ge, and biaxially strained Si with respect to [100] axis, which represents behavior of diamond–like lattices under non–isotropic strains.

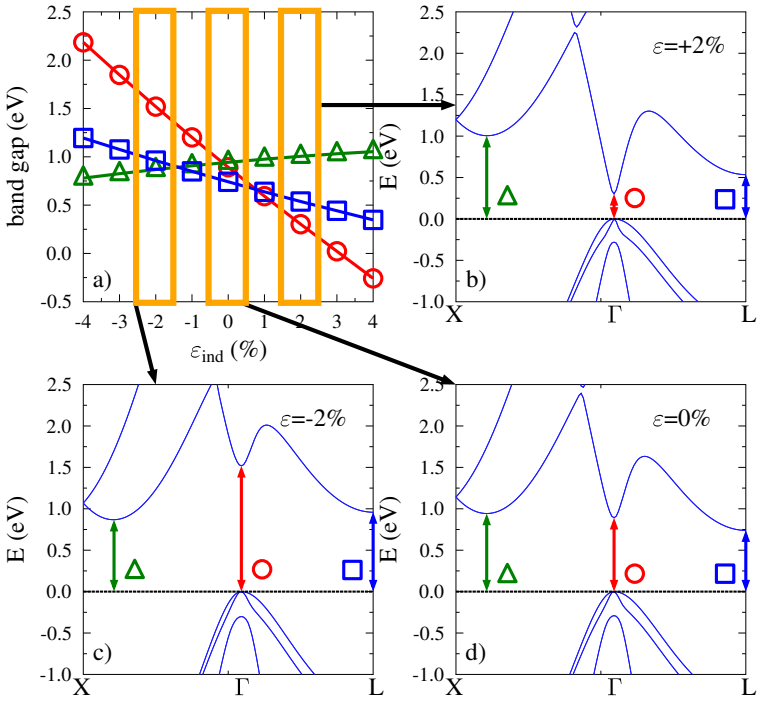

Figure 2.7: Pictorial diagram of the band gaps presentation, on the example of isotropically strained Ge. a) shows how band gaps change with strain, while b), c) and d) visualize band structures under given stains.

In the first case (Fig. 2.8 a,b,c) three situations can be distinguished:

a) at a range of strain represented here by -6% compressive strain, the open direct band gap exists, with Γ_7^- (irreducible representation) CB minimum, degenerate VBM Γ_8^+ and SO split-off band Γ_7^+,

b) at a range of strain represented here by -4% compressive strain the direct gap is closed, Sn becomes semi–metallic, and the Γ_7^- point goes below the degenerate Γ_8^+ (negative direct band gap),

c) at a range of strain represented here by -1% compressive strain, Γ_7^- goes below the split-off band Γ_7^+.

In the case b) and c) it may happen that certain region of CB goes below the Fermi level and then Sn becomes a metal. Similar situation can be observed in Ge (although at different ranges of strain), as well as in GeSn alloy, at specific composition/strain ranges [63]. In the second case (Fig. 2.8 d,e,f) also the three typical situations appear:

d) at a range of strains (biaxial, with respect to [100]), represented here by -4% compressive strain, the degeneracy of HH and LH bands is removed (due symmetry break) and inversion of HH and LH bands appears,

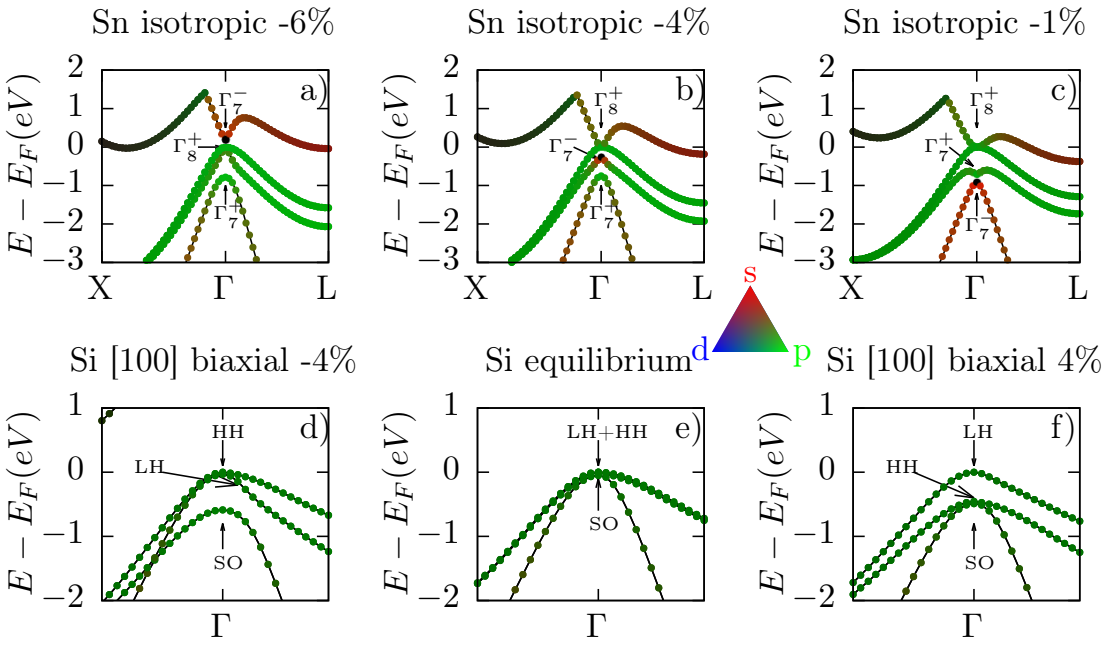

Figure 2.8: Typical qualitative features of bands behavior as a function of strain for diamond-like group IV crystals, on the example of isotropically strained Sn in a) -6% b) -4% and c) -1% , and biaxially strained Si with respect to [100] direction Si in d) -4%, e) 0% (equilibrium structure) and f) 4%. "Fat bands" representation is used, i.e. the color stands for the kind of orbital and the intensity for the relative contribution; the green colour denotes p atomic orbital and red - s orbital; the values of gaps are not correct because the calculations have been done with the LDA functional (PAW atomic data), and the known deficiency of DFT (the band gap problem) is exhibited.

e) at equilibrium lattice constant, there is a quite big direct band gap (about 2.3 eV), degenerate at Γ HH and light hole LH bands, and slightly detached SO split-off band; in this case Si (and also C) the isotropic strain results only in the vertical movement of bands and no inversion is observed,

f) at a range of strains, represented here by +4% tensile strain, the degeneracy of HH and LH bands is removed but no band inversion takes place.

It should be stressed out that the values of the band gaps given above were calculated with LDA functional, and therefore are not correct. They are here only for schematic representation of the behavior of the bands and their symmetries under strain. The expected correct values are given in Fig. 2.10a and Tabs. tables 2.7 to 2.11, where the mBJLDA functional has been used.

The defined above gaps as functions of strain, for all systems and all applied strains are presented in Fig. 2.10a and Tabs. tables 2.7 to 2.11, whose meaning is explained in Fig. 2.7. A striking feature of almost all the plots (except for isotropic case) is a sharp change in the value of the linear coefficient between the tensile and

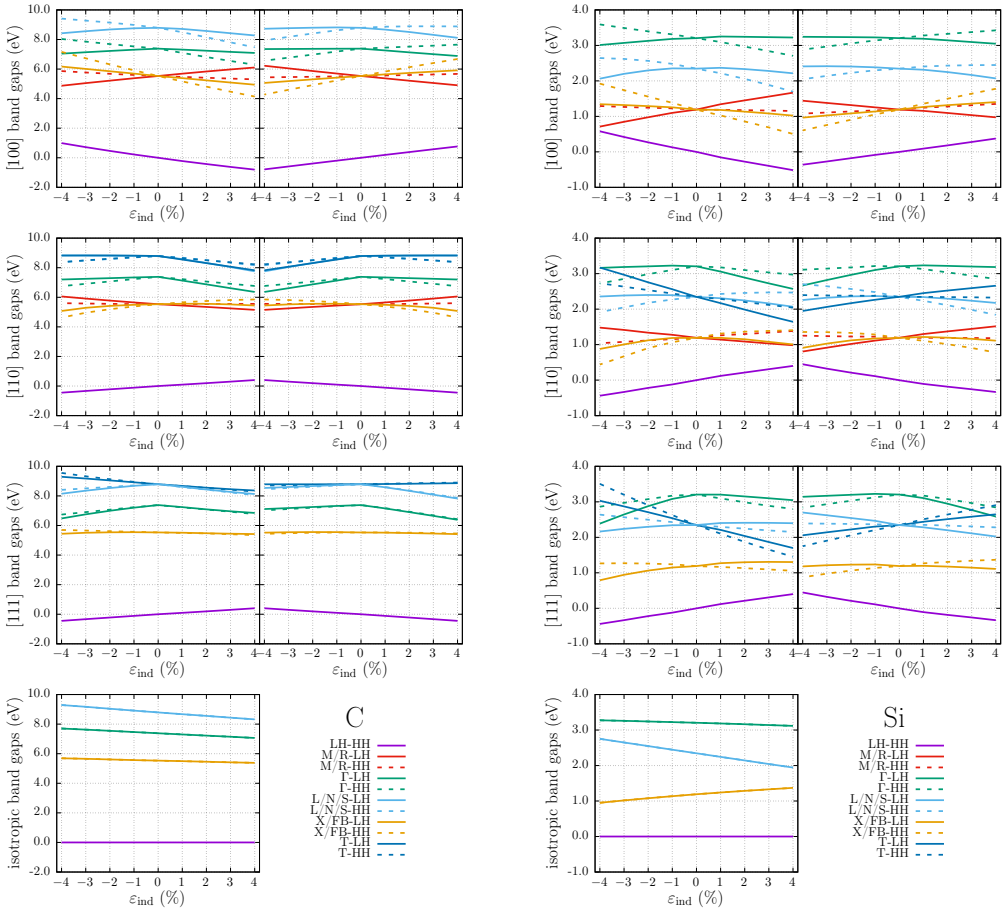

(a) (b)

Figure 2.9: Band gaps in diamond–like crystal. Bottom–left graph – isotropic strain; Above – left column: biaxial strain, right column: axial strain. From the first to the last row, respectively: strains with respect to directions [100], [110], [111]. Purple line is the difference between light and heavy hole bands, green lines are direct band gaps, red and orange are indirect band gaps (Γ-X), blue are indirect band gaps (Γ-L). Dashed lines are with respect to the top of the heavy hole band, continuous to the top of the light hole band.

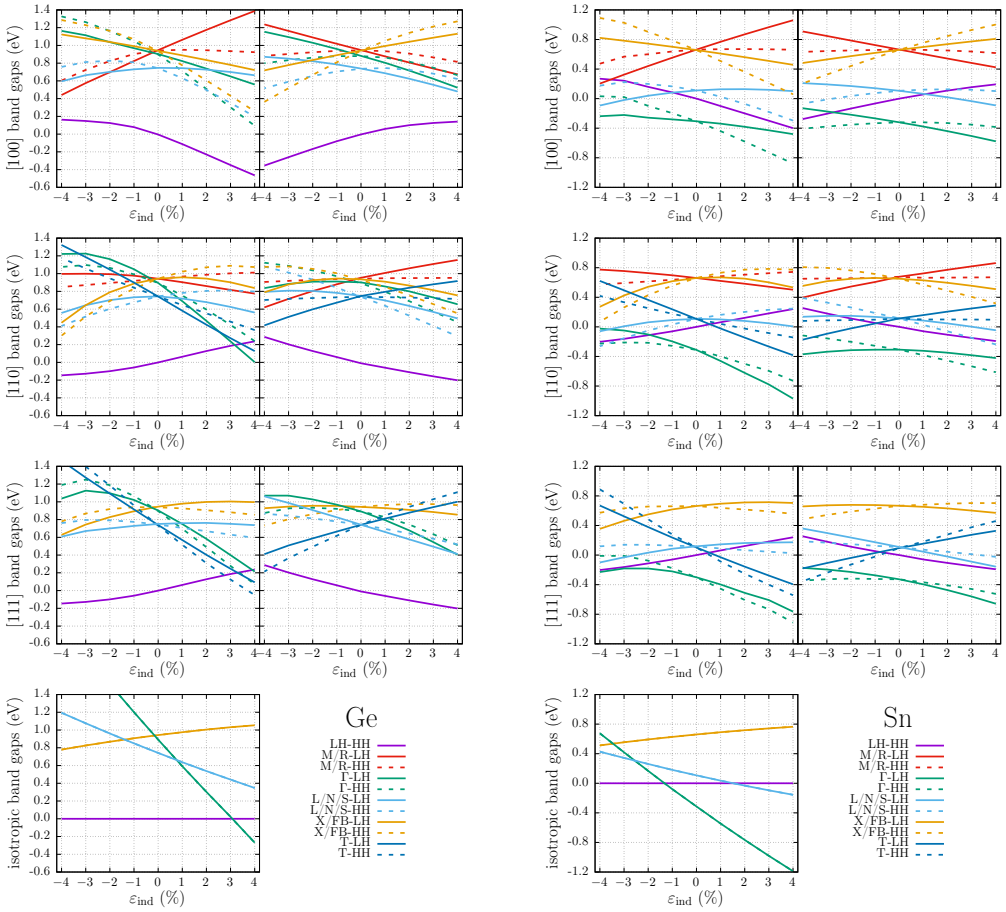

(a) (b)

Figure 2.10: Band gaps in diamond–like crystal. Bottom-left graph – isotropic strain; Above – left column: biaxial strain, right column: axial strain. From the first to the last row, respectively: strains with respect to directions [100], [110], [111]. Purple line is the difference between light and heavy hole bands, green lines are direct band gaps, red and orange are indirect band gaps (Γ-X), blue are indirect band gaps (Γ-L). Dashed lines are with respect to the top of the heavy hole band, continuous to the top of the light hole band.

the compressive strain (even its sign) at the zero strain point. As it has been already explained the reason for such behavior is the inversion of HH and LH bands, as demonstrated in Fig. 2.8 (d,e,f). This is due to the opposite direction of movements of HH and LH bands at applied compressive and tensile strains (see Tab. 2.6). The only situation at which this not happens is the isotropic strain, and here the change of gaps is monotonic in the full range of strain. Various behavior of bands in directions from Γ to X and L star points (Δ and Λ lines, respectively) has been observed due to strain induced symmetry breaking, which is a known feature, and the appropriate distinction is made in Tabs. tables 2.7 to 2.11. Another rather obvious feature is that the plots for tensile and compressive strains are qualitatively similar except they are "reflected" with respect to zero–strain vertical line. This is because applying the biaxial/axial compressive strain leads to the qualitative change in the structure the same as under the axial/biaxial tensile strain. The changes in the structures under biaxial strains are more pronounced than under axial ones, because the Poisson ratios are higher, and that is why the changes in the gaps are bigger. Another distinct feature is that in most cases the changes in the gaps are almost linear. There are, however, some exceptions, like direct band gaps in Ge at [110] and [111] case where big bowings at compressive strains can be seen. From applications point of view the most interesting are the cases where indirect–direct gap transition induced by strain appears, which in the case of Ge takes place in almost all biaxial strains (except [111]) as well as at isotropic strain. Also in Sn at uniform compressive strain a direct open gap appear. It should be mentioned that strain is often applied jointly with mixing of elements (alloying) (see e.g. [63]), which opens large opportunities of band structure formations towards wanted in particular applications features.

Table 2.7: Equilibrium band gaps (eV) and the linear coefficients of gap changes (eV/%) for isotropic strains.

		$\Gamma-\Gamma$	$\Gamma-X$	$\Gamma-L$
C	gap	7.38	5.53	8.79
	lin. coef.	-0.08	-0.04	-0.12
Si	gap	3.20	1.32	2.34
	lin. coef.	-0.02	0.06	-0.10
Ge	gap	0.89	0.94	0.74
	lin. coef.	-0.30	0.04	-0.11
Sn	gap	-0.31	0.66	0.11
	lin. coef.	-0.23	0.03	-0.08

Both band structures and orbital compositions were calculated for all considered systems. Although not shown here, the database of this results is kept, and can be shared on request.

A good verification of presented here results is their comparison with available experimental data [29, 67, 76, 83], presented in below (Fig.2.11). As it can be seen, for the LH–HH splitting the agreement is excellent. Also for direct gap in

Table 2.8: Linear coefficients of band gap changes for axial compressive strains (eV/%).

gap	C	Si	Ge	Sn
$\Gamma - \Gamma\,[100]$	0.20	0.08	0.02	-0.07
$\Gamma - X\,[100]$	0.02	0.03	0.02	-0.06
$\Gamma - M\,[100]$	0.31	0.15	0.14	0.04
$\Gamma - N\,[100]$	0.21	0.07	0.06	-0.03
$\Gamma - \Gamma\,[110]$	0.26	0.14	0.01	-0.06
$\Gamma - X\,[110]$	0.02	0.07	0.03	-0.04
$\Gamma - R\,[110]$	0.10	0.10	0.08	0.01
$\Gamma - T\,[110]$	0.24	0.10	0.08	0.01
$\Gamma - S\,[110]$	0.26	0.02	-0.01	-0.07
$\Gamma - \Gamma\,[111]$	0.09	0.09	0.003	-0.04
$\Gamma - FB\,[111]$	0.02	0.08	0.05	0.002
$\Gamma - L\,[111]$	0.09	-0.01	-0.03	-0.06
$\Gamma - T\,[111]$	0.02	0.15	0.13	0.07

Table 2.9: Linear coefficients of band gap changes for axial tensile strains (eV/%).

gap	C	Si	Ge	Sn
$\Gamma - \Gamma\,[100]$	-0.13	-0.05	-0.09	0.05
$\Gamma - X\,[100]$	-0.16	-0.06	-0.07	-0.011
$\Gamma - M\,[100]$	0.09	0.05	0.05	0.09
$\Gamma - N\,[100]$	-0.17	-0.08	-0.06	-0.0008
$\Gamma - \Gamma\,[110]$	-0.16	-0.09	-0.11	0.04
$\Gamma - X\,[110]$	-0.22	-0.1	-0.09	-0.04
$\Gamma - R\,[110]$	0.02	-0.002	0.002	0.05
$\Gamma - T\,[110]$	-0.10	-0.005	-0.006	0.04
$\Gamma - S\,[110]$	-0.10	-0.13	-0.11	-0.04
$\Gamma - \Gamma\,[111]$	-0.25	-0.16	-0.12	0.03
$\Gamma - FB\,[111]$	-0.03	-0.03	-0.02	0.01
$\Gamma - L\,[111]$	-0.24	-0.09	-0.08	-0.03
$\Gamma - T\,[111]$	0.02	0.07	0.06	0.09

Table 2.10: Linear coefficients of band gap changes for biaxial compressive strains (eV/%).

gap	C	Si	Ge	Sn
$\Gamma - \Gamma\,[100]$	0.09	0.06	-0.07	-0.06
$\Gamma - X\,[100]$	0.17	0.13	0.13	0.05
$\Gamma - M\,[100]$	-0.16	-0.03	-0.06	-0.1
$\Gamma - N\,[100]$	0.10	0.08	0.04	-0.01
$\Gamma - \Gamma\,[110]$	0.16	0.12	-0.05	-0.05
$\Gamma - X\,[110]$	0.22	0.19	0.16	0.10
$\Gamma - R\,[110]$	0.02	0.04	0.02	-0.03
$\Gamma - T\,[110]$	0.10	-0.10	-0.11	-0.13
$\Gamma - S\,[110]$	0.10	0.11	0.08	0.04
$\Gamma - \Gamma\,[111]$	0.23	0.21	-0.04	-0.05
$\Gamma - FB\,[111]$	0.02	0.11	0.08	0.02
$\Gamma - L\,[111]$	0.16	0.05	0.03	-0.001
$\Gamma - T\,[111]$	-0.12	-0.16	-0.18	-0.20

Table 2.11: Linear coefficients of band gap changes for biaxial tensile strains (eV/%).

gap	C	Si	Ge	Sn
$\Gamma - \Gamma\,[100]$	-0.27	-0.13	-0.20	0.10
$\Gamma - X\,[100]$	-0.06	-0.01	-0.005	0.10
$\Gamma - M\,[100]$	-0.35	-0.17	-0.17	-0.05
$\Gamma - N\,[100]$	-0.33	-0.16	-0.14	-0.002
$\Gamma - \Gamma\,[110]$	-0.26	-0.16	-0.22	0.06
$\Gamma - X\,[110]$	-0.02	-0.05	-0.03	0.03
$\Gamma - R\,[110]$	-0.10	-0.05	-0.04	0.02
$\Gamma - T\,[110]$	-0.24	-0.18	-0.15	-0.06
$\Gamma - S\,[110]$	-0.26	-0.07	-0.05	0.03
$\Gamma - \Gamma\,[111]$	-0.15	-0.10	-0.21	0.03
$\Gamma - FB\,[111]$	-0.05	-0.03	-0.02	0.01
$\Gamma - L\,[111]$	-0.18	-0.05	-0.04	0.01
$\Gamma - T\,[111]$	-0.12	-0.22	-0.20	-0.12

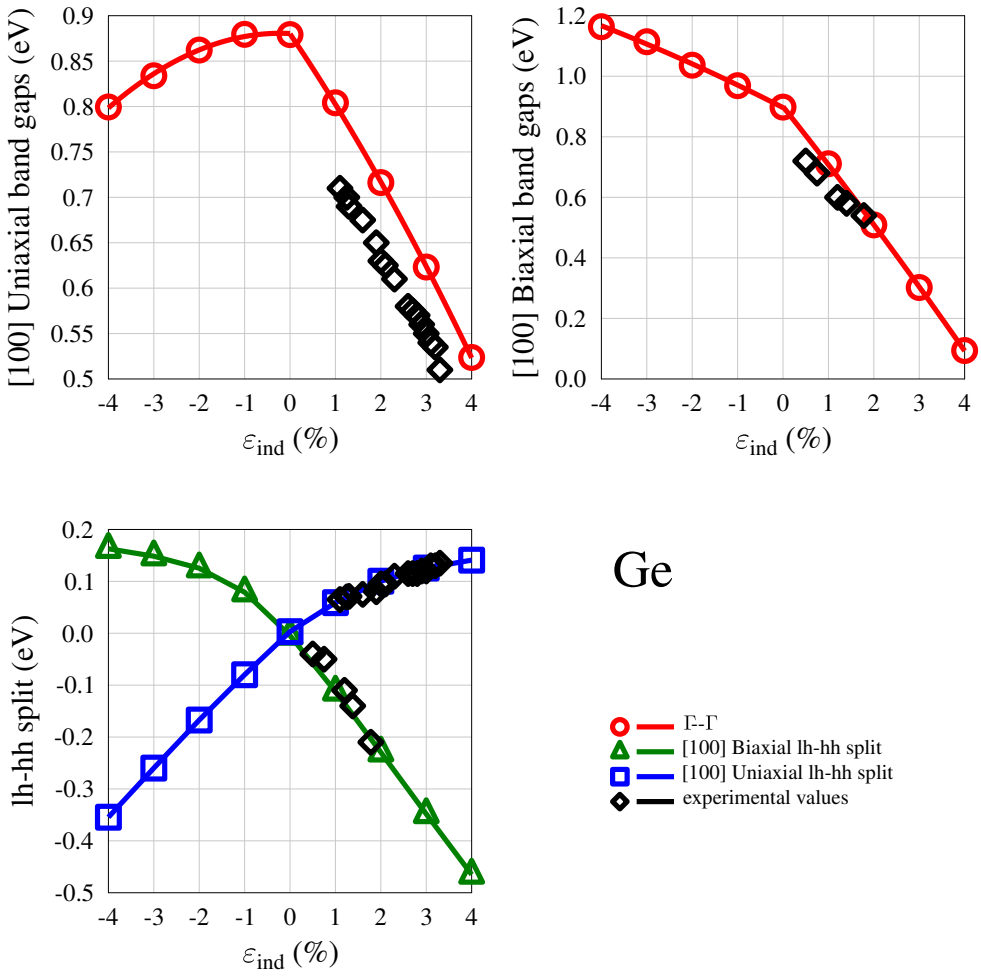

Figure 2.11: Computational results vs. experimental data for germanium; upper left panel: direct gap [100] axial strain (according to [29]), upper right panel: [100] biaxial [76] (the reductions of the experimental direct gaps are induced by temperature, $300K$), bottom panel: [100] biaxial strain LH-HH[83], [100] axial LH-HH[67].

Ge the agreement is very good, taking into account the fact that the measurement was performed at room temperature, whereas the calculations correspond to zero temperature. Considering about 10% temperature induced reduction in the band gap at $300K$ (tabular value) makes the agreement of obtained results with experiment very good. Finally, the reported in [75] indirect–to–direct band gap crossing point at 1.94% [100] biaxial strain agrees very well with given prediction (see Fig. 2.10a). The presented below comparison strongly point at credibility of the provided computational results, since, the calculations are consistent regarding the methods applied.

2.2.3 Deformation potentials

To have a complete image of the electronic band structure behaviour under strains the deformation potentials a_v, a^{dir}, a^{ind}, b, d, Ξ_u^{Δ}, Ξ_u^{L}, as defined defined in [89], have been calculated. The deformation potentials are the parameters describing the strain induced characteristic energies variation. The results are gathered and compared with the literature data in Tab. 2.12. The main conclusion from the presented data is that the values of the relative deformation potentials (describing the changes in energy differences) agree well with the literature data, whereas the absolute ones (describing the changes in energies given with respect to the absolute energy reference point) differ significantly. At this stage explanation of the variation in results remains unknown, however, in [93] an experimental value of $a_v = -12.7$ eV for Ge, and in [7] a theoretical values for Ge of $a_v = -12.4$ eV and for Si $a_v = -10.2$ eV are reported. These number differ significantly from those quoted in Tab. 2.12, which means that even in the literature there is a big discrepancy of data. In this work the calculation procedure is precisely described (see Sect. 2.1) which establishes a frame for future discussion.

Table 2.12: Deformation potentials.

	Si	Si ref.	Ge	Ge ref.
Δ_0	0.05	0.04 [89]	0.29	0.30 [89]
a_v	-0.30±0.43	2.46 [89]	-4.0±0.55	1.24 [89]
b	-1.39±1.03	-2.35 [89]	-6.72±0.90	-2.55 [89]
d	-0.37±1.01	-5.32 [89]	-10.00±3.19	-5.50 [89]
a^{dir}	-0.65±0.02	-0.48 [89]	-9.59±0.42	-9.48 [89]
a^{ind}	1.74±0.05	1.72 [89]	-3.53±0.05	-2.78 [89]
Ξ_u^{Δ}	8.80±0.09	8.70 [89]	9.50±0.10	9.02 [55]
Ξ_u^{L}	14.30±0.04	13.85 [55]	15.70±0.20	16.30 [89]

2.2.4 Effective masses

There are rather few results in the literature of the theoretical calculations of effective masses and, in particular, their dependencies on strains. Some calculations using various methods, *ab initio*, TB, $\mathbf{k} \cdot \mathbf{p}$, are reported eg. in [9, 70, 90]. In this work a systematic first principles computational study has been performed of chosen effective masses dependence on strains, using the method described in Sect. 2.1. The results are presented in Figs. figs. 2.12a, 2.12b, 2.13a and 2.13b.

Before we start the discussion, it should be pointed out that the data provided agree well with those reported in [9, 70, 90] and experimental values referenced there (see Tab. 2.13). This fact enhances the credibility of the results and the discussion of the effect of strains.

First, it should be noted that in all the dependencies presented in Figs. figs. 2.12a, 2.12b and 2.13a, as expected, the qualitative behaviors for biaxial and axial strains are inverse with respect to zero strain, for the reason discussed previously. One

Table 2.13: Effective masses (in units of electron mass) in chosen BZ points calculated in this work and compared with the literature reference data. 'h' stands for holes.

	m_{eff}	this work	GW [70]	EPM [70]	$\mathbf{k}\cdot\mathbf{p}$ [70]	TB [9]	DFT [90]	expt.
Si	Γ [Δ]	0.676					0.158	
	Γ [Λ]	0.514						
	X	0.798	0.925	0.89	0.928	0.891	0.915	0.916 [70]
	L	1.92	1.8083	1.855	1.704	3.433		2.0 [9]
	h [Δ]	0.327				0.276	0.22	0.275 [9]
	h [Λ]	0.811				0.734	0.66	0.738 [9]
Ge	Γ [Δ]	0.047					0.037	0.038 [90]
	Γ [Λ]	0.05						
	X	0.674	0.881	0.964	0.874	0.701		0.9 [9]
	L	1.69	1.626	1.763	1.59	1.584	1.66	1.58 [70]
	h [Δ]	0.236				0.173		0.211 [9]
	h [Λ]	0.602				0.531		0.502 [9]

can distinguish a few characteristic cases of different qualitative behavior. In the conduction band, for example, a very big increase in the Si effective mass can be observed, at Γ in $\Gamma - X$ direction, with [100] axial tensile (or biaxial compressive) small (1%) strain. Such a behavior is connected with "flattening" of the band, and what is interesting, this does not happen in the Γ-L direction. A large increase can also be seen at X under [110] strains, both in Si and Ge, but at higher strains $(3-4\%)$, and at X under [111] strains. On the other hand, very small effective masses (0.04 at equilibrium) can be found in Ge at Γ, but an interesting fact is that at some strains ([110] biaxial, [111] biaxial, isotropic) the effective mass clearly tends to zero, which is connected with closing the direct gap, and results in high mobility of CB electrons which has a practical meaning. Apart from that there is a variety of cases where the change in the effective masses is regular but not very big (up to 100%, like at [110] strains in Si) or looks almost constant but is irregular (like at X [100] strain, both in Si and Ge), which must be due to numerical noise (the results are extremely sensitive to any numerical uncertainties). In the VB the effective mass behavior is very spectacular because a described previously inversion of bands. Thus, a sudden drop or increase of the effective mass is observed, depending on which band (HH or LH) is actually on the top. The most spectacular change (by one order of magnitude) caused by this effect can be seen in Si isotropic strain.

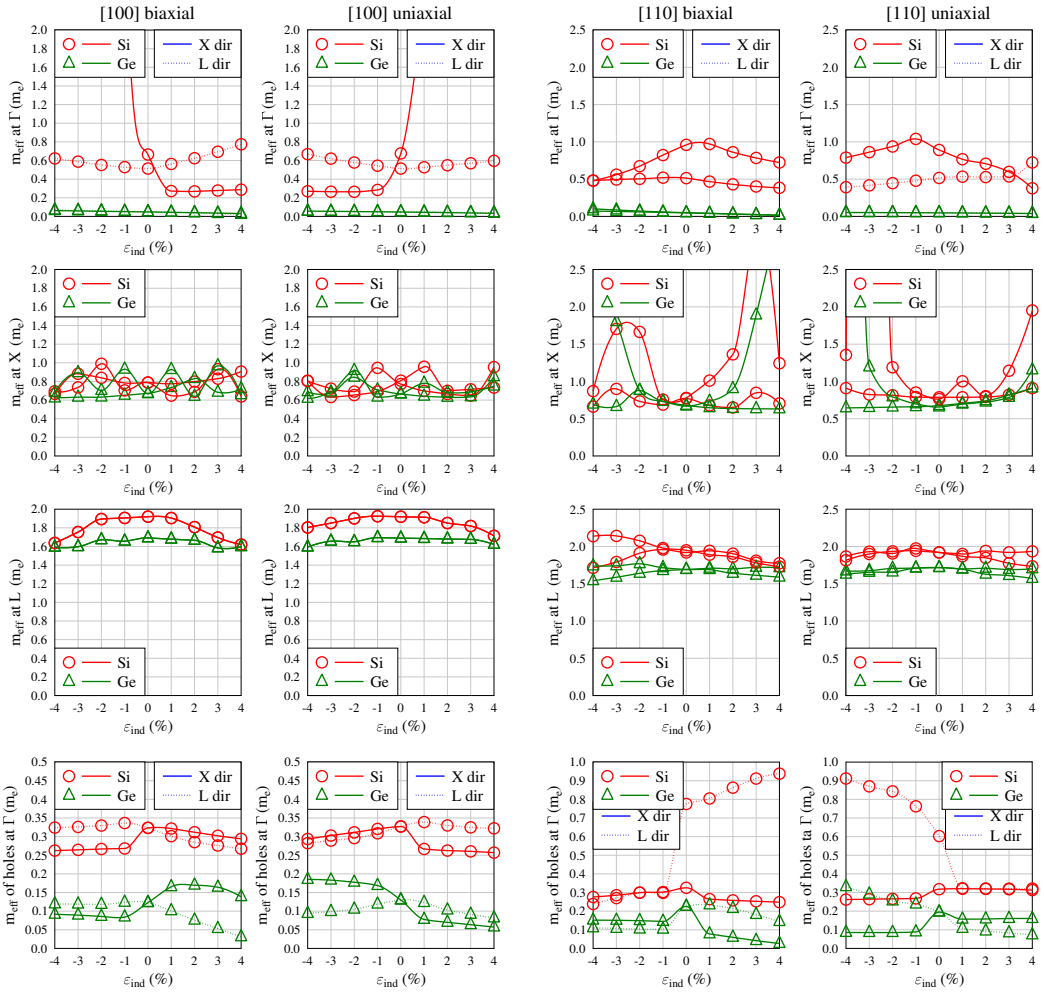

(a) Effective masses dependent on strains with respect to [100] axis; red circles - Si, green triangles - Ge; at Γ: solid line - Γ-X direction, dotted line - Γ-X direction.

(b) Effective masses dependent on strains with respect to [110] axis; red circles - Si, green triangles - Ge; at Γ: solid line - Γ-X direction, dotted line - Γ-X direction.

Figure 2.12

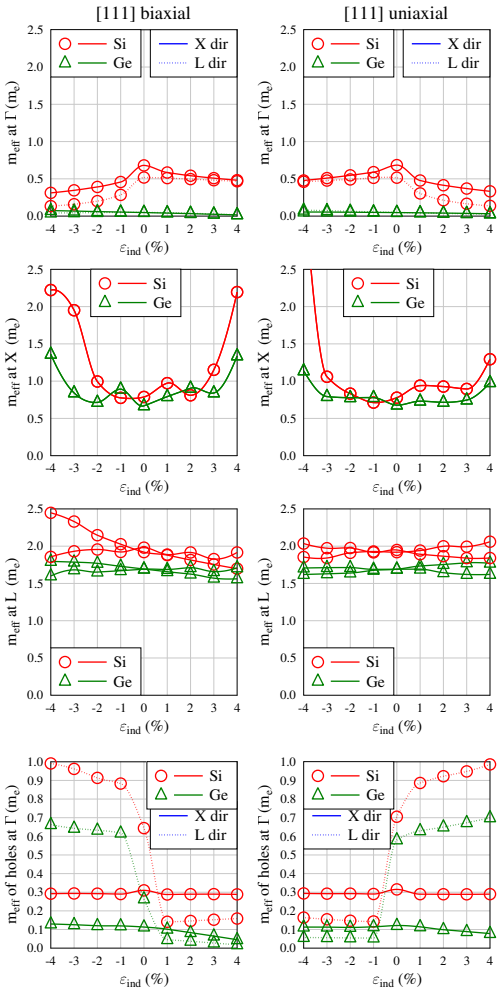

(a) Effective masses dependent on strains with respect to [111] axis; red circles - Si, green triangles - Ge; at Γ: solid line - Γ-X direction, dotted line - Γ-X direction.

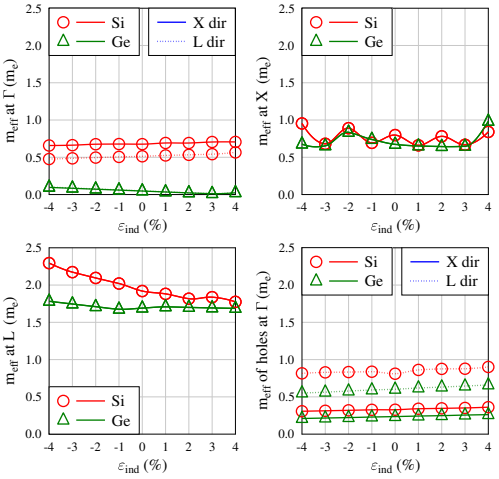

(b) Effective masses dependent on isotropic strains; red circles - Si, green triangles - Ge; at Γ: solid line - Γ-X direction, dotted line - Γ-X direction.

Figure 2.13

2.2.5 Charge carriers mobility

In addition to calculation of effective masses, the effect of strain on carrier mobility has been estimated. The mobility is related to effective mass by scattering time, as follows

$$\mu = \frac{q}{m^*}\bar{\tau}, \tag{2.8}$$

where q is an elementary charge, and $\bar{\tau}$ is the average scattering time. The scattering time, in general, depends on many factors connected with the scattering mechanisms which is not considered here. Instead, an empirical model based on Monte Carlo simulations was used to evaluate the average scattering time for electrons [26]:

$$\begin{aligned}\bar{\tau}_n =& \tau_0 + \tau_1 \cdot exp\left(C_1 \cdot \left(\frac{T_n}{300K} + C_0\right)^2 + \right. \\ &\left. + C_2 \cdot \left(\frac{T_n}{300K} + C_0\right) + C_3 \cdot \left(\frac{T_L}{300K}\right)\right)\end{aligned} \tag{2.9}$$

where T_n is the electron temperature, T_L is the lattice temperature, while all of the τ and C are material dependent constants (shown in Tab. 2.14). Formula 2.9 has been used here for calculating the scattering time of electrons. In the case of holes the scattering time is independent of carrier and lattice temperatures:

$$\bar{\tau}_p = \tau_2. \tag{2.10}$$

Table 2.14: Material parameters for average scattering time (Eq. 2.9) [26]. τ are given in (ps).

	τ_0	τ_1	C_0	C_1	C_2	C_3	τ_2
Si	1	-0.538	0	0.0015	-0.09	0.17	0.4
Ge	0.26	1.49	0	-0.434	1.322	0	0.4

For given temperatures, the mobility changes are completely established by effective mass (Eq. 2.9). For unstrained materials the mobilities for both electrons and holes are known. For Si it is $\leq 1400\frac{cm^2}{V\cdot s}$ and $\leq 450\frac{cm^2}{V\cdot s}$ for electrons and holes respectively, and for Ge similarly $\leq 3900\frac{cm^2}{V\cdot s}$ and $\leq 1900\frac{cm^2}{V\cdot s}$ (according to NSM Archive [56]). If we assume that the strain does not affect the scattering time, the strain dependent mobilities can be evaluated. Examples of such calculations are presented in Fig. 2.14. First of all one can see that presented results agree well with tabular data at equilibrium state. It can be also observed that the strain induced changes in effective masses affect significantly the mobilities. In extreme cases they can change even by an order of magnitude.

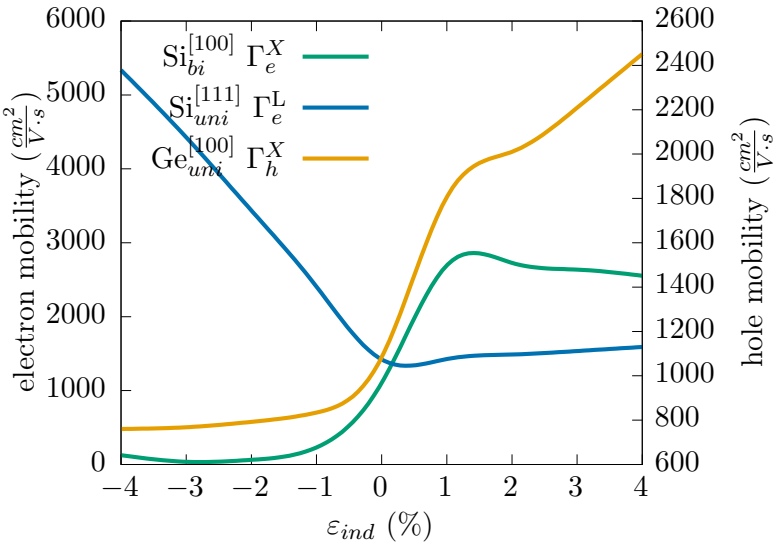

Figure 2.14: Carrier mobility examples calculated for T_n, $T_L = 300K$.

2.2.6 Precision and accuracy of the results

When DFT results are presented the question about their precision and accuracy always arises. The term "precision" in this context refers to the precision of calculations at given methods used within DFT, i.e. their deviation from the exact result if it existed. Since the "exact" result does not exist, the only way of estimating the precision is to compare the results with analogous ones, given by other codes, among which the full potential implementations seem to be most credible. This issue is widely discussed in [45] where a special parameter Δ is introduced as a measure of discrepancy between EOS for a sample of crystals calculated by a given pair of codes. This parameter, when used in reference to full potential codes becomes a measure of precision.

In turn, the term "accuracy" refers to the agreement of computational results with experimental data, and it seems that an ultimate criterion to value various DFT methods/codes is to compare the results with the experiment. In the light of these remarks the discussion of the results presented is conducted below.

The table in Fig.4 in [32] shows a comparisons of Δ parameter for most known DFT methods, in reference to full–potential methods. The PAW JTH/ABINIT, used in this work (in even newer version than in [32]), has there a very good (0.6) value. Only VASP and various full potential codes show slightly better values (the lowest average value is 0.5 and the highest is 13.3). In the results presented here, this kind of PAW datasets has been used in all the structural calculations and in the case of deformation potentials as well. Taking into account that the rigorous convergence tests have been performed, the precision of presented results should be high. Regarding the accuracy, it is also very satisfactory, as shows the comparison with the available experimental data. E.g. Tab. 2.1 shows an excellent agreement of the calculated lattice constants with experimental ones. Also the elastic constants, although defined here in an unconventional way, when transformed to the standard

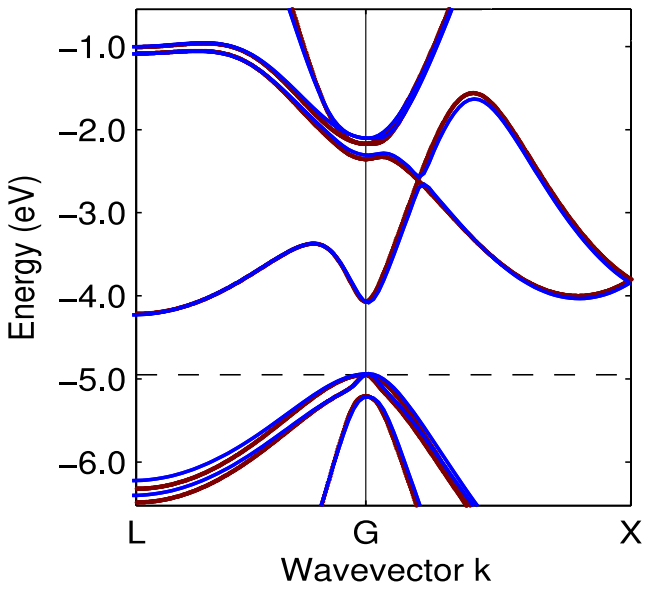

Figure 2.15: Comparison between Wien2k (red line) and ABINIT with mBJLDA (blue line) band structure of Ge in equilibrium state.

ones agree well with the textbook data (see Tab. 2.5).

The calculations of band energies, gaps and effective masses have been performed using different method (HGH joined with the mBJLDA XC potential, see Sect. 2.1), and thus require a separate discussion of precision and accuracy. As described in Sect. 2.1, the mBJLDA c_TB09 parameter (called here c) has been fitted to get correct (experimental band gaps) and specially treated for strained systems (Eq. 2.5). Figure 2.15 shows a comparison of Ge band structure obtained in this work and by Wien2k code. And one can see that the agreement is very good. This means that conducted calculations are expected to be highly precise. As far as the accuracy is concerned the agreement with the available experimental data shown in Fig. 2.11 is very good.

The accuracy of effective masses is an important issue to comment, since this is a known fact that the mBJLDA functional overestimates effective masses by $20-30\%$ [38], which is then a systematic error. Surprisingly the approach used in this work does not quite reflect this tendency. As Tab. 2.13 shows, the effective masses calculated here (in a very strict mathematical approach) sometimes are even lower than the experimental ones, but the overall agreement is quite satisfactory. Nevertheless, the results presented here can certainly be regarded as a good qualitative picture (with rather low quantitative uncertainty) of masses vs. strains variation.

The calculations of the deformation potentials, particularly those describing the

absolute changes in energies, are a delicate issue. For the top of VB, they have been done with the use of PAW atomic datasets. The same which gave very satisfactory structural parameters. Here, the DFT band gap problem does not exist since we consider only the VB top energy with respect to the unified energy reference point. Thus, the discrepancy of provided results with the literature data is surprising. For this reason there have been included a precise description of the method used (see Sect. 2.1), so that the reproduction of the data or questioning the approach would be possible.

Chapter 3

Alloying

The second method of band structure engineering which will be discussed here is a formation of the alloys. The papers published on the subject within our research group are [64, 78], although the author of this dissertation contributed only to the second paper ([78]), oriented towards the application of *ab initio* data (from [64]) in device modelling. As it will be explained in the following section a direct application of DFT results in device modelling is very inconvenient and some intermediate representation of the electronic structure must be used. In [78] the 30–bands $\mathbf{k} \cdot \mathbf{p}$ method has been proposed for that purpose and my contribution consisted in preparation of *ab initio* data, via computational alchemy, to be suitable for fitting the $\mathbf{k} \cdot \mathbf{p}$ parameters.

3.1 Computational method

Creating alloys and admixtures of different materials (even slightly) can drastically change materials properties, especially in the case of semiconductors, which are known for their huge sensitivity for impurities. The main difference between alloying and doping is percentage of admixture. It is worth noting that low (light) doping is considered to be, when one dopant atom is added per 100 million atoms, while heavy (high) doping per ten thousand atoms. In an alloy, two (or more components) are mixed at any proportion.

The concept of alloy is quite vast and covers many different material types. From uniform materials to multi–phase ones, including all types of doping in atomic scale. A doping atom can substitute the host material atom or fit in an interatomic position. That gives a large field of study. In this work only a uniform phase with substituting the host material is taken under consideration. It is also assumed that the atoms distribution is perfectly random, which in *ab initio* calculations with the supercell approach is emulated by the so called special quasirandom structure (SQS), described below.

The active region of modern optoelectronic devices (detectors, light emitting diodes, lasers, etc.) is often based on semiconductor alloys. They offer an opportunity of tuning the band gap by varying their composition. One of materials of interest in the field is the $Ge_{1-x}Sn_x$ alloy [14, 34, 47, 87, 95]. Its direct gap can be tuned in the range of $0.89 - 0$ eV by varying the composition [64, 81, 91, 99]. Additionally, it

exhibits an interesting property, where by varying the alloy composition, a transition from indirect to direct band gap takes place. This transition appears at a relatively small admixture of Sn in Ge (around 6.5%) (e.g. [64]). This feature, joined with the observed high mobility of carriers, makes this material a promising candidate for optoelectronic applications. This fact has been a reason for an intensive experimental and theoretical investigations of this material, e.g. [1, 3, 10, 12, 13, 16, 18, 20, 31, 35, 43, 44, 51, 59, 64, 66, 73, 80, 81, 91, 94, 96, 97, 99, 100]. In particular a number of DFT based *ab initio* theoretical studies have been conducted [10, 12, 18, 20, 35, 44, 51, 59, 64, 66, 73, 80, 94, 97, 99, 100].

It is a known fact that the *ab initio* methods provide very realistic predictions of properties of atomic systems. In the case of alloys, the method of choice is the use of periodically repeated supercells containing up to a few hundred atoms of species forming the system, which makes the calculations computationally challenging [18, 64, 66, 100]. The most prominent advantage of this method is the ability to take into account the lattice distortion around impurities, vacancies and interatomic position dopants. However, in such an approach only a discrete number of compositions can be analyzed. Moreover, the problem emerges, even if big supercells are used, that the system is always cell–periodic, which seems to be far from the perfectly random alloy which is the subject of analysis. Nevertheless, within the supercell approach we can emulate to some extent the perfectly random alloy by applying the SQS (Special Qausirandom Structures) [101] technique. In principle, the technique consists in choosing the atomic positions in the supercell in such a way that the correlations between the numbers of atoms of the same kind in subsequent coordination zones are as close to the known correlations in the perfectly random structure as possible. Obviously, the bigger is the supercell the better is the approximation, but also the bigger is the computational cost, and thus some compromise must be established.

Another inconvenience appearing when large supercells are used are numerous folded bands which makes the interpretation of the picture of the band structure rather complicated. The necessary unfolding procedure [72] provides an effective band structure represented in the form of spectrally weighted eigenvalues, which are torn and blurred at some compositions. This, and also big size of the wave function files, makes the direct application of supercell representation of the band structure in modeling of semiconductor devices very inconvenient. For this reason, in device modeling other representations of electronic bands are most often used, among which the $\mathbf{k} \cdot \mathbf{p}$ method seems to be the most popular [19, 24, 25, 46, 69]. These methods require certain number of parameters which are found from fitting either to experimental data or to large scale *ab initio* calculations.

In [78], to which the author of this dissertation contributed, an approach which joins large scale *ab initio* calculations with 30–bands $\mathbf{k} \cdot \mathbf{p}$ method is applied. The latter method is known to correctly reproduce the electronic band structure in the full BZ. The approach allows to find the values of the parameters used in the $\mathbf{k} \cdot \mathbf{p}$ method. Finding them directly from *ab initio* supercell data would be difficult (if possible at all), due to the character of the obtained band structures. Therefore, it is proposed to make an intermediate step which is based on other *ab initio* approaches.

Apart from the supercell method there are basically three other methods suitable

for alloy modeling. First, and the simplest one, is the Virtual Crystal Approximation [4] (VCA) which in principle relies on the linear interpolation of band energies of component materials. The approximation is very crude, in particular it is not able to reproduce the band gap bowings, often present in the alloys (particularly the highly mismatch ones), and being a result of local lattice distortions. The advantage of this method is the low computational cost. However, VCA was a useful starting point to create some modified methods, suitable for specific group of materials [65, 68].

The second approach is so–called Coherent Potential Approximation (CPA). It is physically the most sophisticated method and is supposed to model adequately the scattering properties of disordered system. This approach is appropriate for Green's function formalism, in which KKR method is implemented. Unlike VCA, the CPA instead of mixing potentials, it mixes, at given proportion, the Green's functions of the component crystals to form an alloy Green's function. That way, it approximates a configurationally random alloy with an effective medium that is determined self–consistently from the condition of stationary scattering. On the other hand, it is insufficient for the geometry optimisation or for the total energy calculations. Due to that, the impurities which highly distort lattice will not be well represented.

The third method available is called the Computational Alchemy and consists in superposition of pseudopotentials on atomic level. In that way a kind of alchemical atom is formed which represents the scattering properties of composing atoms at a given proportion. Then the ideal periodic structure is formed from the alchemical atoms, and this is the main shortcoming of the method: it is not able to reproduce the local lattice distortions, which are due to different sizes of atoms composing the alchemical atom.

Because the CPA method requires Green's function approach and as an output gives Bloch's spectral function instead of typical band structure, that method also was rejected for device modeling purpose. On the other hand VCA is not accurate enough. Thus, in this work, a computational alchemy was chosen.

The approach has already been exploited in a number of works, e.g. [5, 17, 49, 74]. The ABINIT package was used with implementation of the computational alchemy, called the Alchemical Mixing (AM). The AM itself is known to provide rather poor description of electronic structure, particularly for highly mismatched alloys (HMA), mainly because it does not account for the local distortions of the lattice [79]. However, when used as a model containing additional fitting parameters it is able to accurately reproduce the band structure for any composition of an alloy at low computational costs. Thus, at the first step, the AM method is used to approximate the reference supercell unfolded band structures. Next, the continuous AM bands are used to find the values of the parameters of 30–band $\mathbf{k} \cdot \mathbf{p}$ model, through a specially designed optimization method. As a result, an effective full BZ electronic band structure description of the $Ge_{1-x}Sn_x$ alloy in the full composition range is obtained.

As mentioned above, to approximate the *ab initio* supercell band structure we the concept of computational alchemy has been used, as implemented in the ABINIT

code [28] and called the alchemical mixing (AM) there. The implementation uses the following construction [27]:

- the local potentials are mixed in the proportion given by mixing coefficients,
- the form factors of the non–local projectors are all preserved,
- the scalar coefficients of the non–local projectors are multiplied by the proportion of the corresponding type of atom,
- the characteristic radius of the core charge is a linear combination of the characteristic radii of the core charges,
- the core charge function $f(r/rc)$ is a linear combination of the core charge functions.

In all the linear combinations the mixing coefficients reflect the proportion at which particular atoms enter the alloy are used. In the approach only the atoms with the same valence electronic configuration can be taken (isovalent elements, like e.g. Ge and Sn). In this work the Hartwigsen–Goedecker–Hutter (HGH) pseudopotentials [60] have been used.

There is a lot of freedom in choosing the mixing proportions, the only constrains are that the overall formula $Ge_{1-x}Sn_x$ must be fulfilled at every composition, and that the content of an element in an *alchemical* atom must not be negative. In this work a scheme has been used which, on the one hand, guarantees a consistency of mixing for any composition and, on the other hand, allows, in some extent, to check the effect of mixing proportions on the results. The two *alchemical* atoms representing two sublattices in BZ structure, $A1$ and $A2$, are composed from Ge and Sn atoms according to the formulas:

$$\begin{aligned} A1 &= Ge[(1-x) + \alpha x(1-x)] + Sn[(x) - \alpha x(1-x)] \\ A2 &= Ge[(1-x) - \alpha x(1-x)] + Sn[(x) + \alpha x(1-x)] \end{aligned} \tag{3.1}$$

where α is a parameter responsible for the proportion of mixing and can be varied in the range $[0, 1]$. The mixing parameter α, if non–zero, allows to add a bowing to the mixing curve versus the amount of admixture, and what follows, to not equally occupy chosen site by component atoms. Testing it's impact on results is important. Value of α resembles the arrangement of atoms in supercell. What follows, in larger cells with higher number of independent sites, the obtained results can be sensitive to the choice of mixing parameter.

One of the advantages of the AM approach is a significant reduction of system size to be analyzed from first principles, which can be reduced to a primitive cell. However, the accuracy of such approach is questionable, in particular it does not account for the local distortions of the lattice [79], which is significant in HMAs where the local relaxation effects play a crucial role [62]. Nevertheless, the AM approximation, when used together with supercell calculations [64] as reference, can

be very useful. When properly adjusted to the supercell data, they may provide a very good approximation of electronic bands with continuous curves. Therefore, a procedure of utilizing the AM approach was designed in a way that allows to reproduce results obtained with more accurate methods, including supercell DFT calculations and experimental measurements. In this chapter the applicability of the method is demonstrated with results of DFT supercell calculations serving as reference.

In the AM method there are only two key parameters necessary to achieve realistic band gaps:

1. lattice constant,
2. c (c_TB09) parameter from mBJLDA.

From computational experience we know that the variation of the lattice constant mainly affects the relative energies of CB minima (Γ and L valley), while the variation of the c parameter mainly leads to the movement of the whole CB with respect to the energy axis, and this fact has been utilized in the fitting procedure.

Thus, the fitting procedure was as follows. First, the parameters for the parent crystals (Ge and Sn) were found. The parameters that would give proper band gaps on boundaries (pure Ge and Sn) must be found. In the case of Ge_xSn_{1-x} the parameters could be taken from the strain calculations presented in the previous chapter.

Then, Vegard's law, representing the composition (x) dependence of any physical quantity (O) (including some parameter) with the bowing mediated by the b (bowing) parameter at quadratic term:

$$O^{\mathrm{AB}_{1-x}\mathrm{C}_x} = O(x) = xO^{\mathrm{AC}} + (1-x)O^{\mathrm{AB}} - bx(1-x), \tag{3.2}$$

has been applied to the lattice constant and the c parameter to get proper behavior of direct and indirect band gaps, in particular a proper band gaps crossover composition.

Having the necessary parameters as functions of composition, the band structure calculations can be performed. The procedure for the calculations, as well as estimating the effective masses of charge carriers, is the same as in the case of strain studies that was described in previous chapter.

In all the *ab initio* calculations described in this section the ABINIT package [28] has been used, with LDA, HGH pseudopotentials [27, 60], Perdew and Wang correlation part of the functional [61] (PAW), and the Tran and Blaha modified Becke Johnson functional TB–mBJ (sometimes referred to as mBJLDA) [86] for the exchange part, known for quantitatively improving the electronic band structure while preserving a reasonable time of calculations. As a result of convergence studies, the energy cutoff was set to 60 Hartree, the k–points sampling for BZ integration was $(10 \times 10 \times 10)$ for all the calculations. The energy convergence criteria in the SC run was set to 10^{-9} Ha and the residual wave function convergence criteria in the non–SC part was 10^{-12}. In the investigations the computational alchemy technique has been used.

Table 3.1: Lattice and c parameters achieved from fitting procedure.

parameter	Ge	Sn	b
lattice const. (Å)	10.636	12.25	-1.08
c_TB09	1.037	0.99	-0.02

3.2 Results

3.2.1 Mixing parameter

At the beginning, the effect of the mixing parameter α (Eq. 3.1) on band structure was tested.

The tests performed have shown that the calculated band structures rather weakly depend on the parameter α, namely, when it is varied in the range $[0, 1]$, the maximum band gap variation does not exceed 0.05 eV. Moreover, this effect is overshadowed by the adjusting procedure described in the next section. In provided calculations the value $\alpha = 0.1$ has been used, to assure the symmetry breaking from diamond to BZ, induced by the fact that the alchemical atoms in the primitive cell are not the same. One should note that in the alloy there is no symmetry at all, except for identity, but the BZ symmetry emerging in AM approach has no effect on the results but speeds up the calculations.

3.2.2 AM vs. supercell band structure

As described in the previous section the aim of this work was to reproduce the unfolded supercell band structure with the smooth curves given by DFT AM approximation, in particular a proper behavior of the direct and the indirect band gaps. Two parameters: the lattice constant a and the c (c_TB09) have been found, for the parent materials Ge and Sn, and for the alloy at composition x via the bowing parameter b in Vegard's law 3.2. For practical reasons only the range up to $\approx 30\%$ (closing the band gap) has been considered in this work. As a reference the data from [64] have been used. The results are given in Tab. 3.1.

In Fig. 3.1 the AM and the DFT supercell band gaps ([64]) variations, direct and indirect, are compared, and it can be seen that in the range of composition of interest the agreement is very satisfactory, the discrepancy is not higher than 0.03 eV.

To validate the method even more, in Fig. 3.2 the band structures for parent materials, Ge and Sn, and the unfolded GeSn alloy band structures for chosen compositions (from [64]) are compared with those obtained in this work. It can be seen that the smooth AM curves provide a very good approximation for the supercell bands.

Finally, the effective masses of electrons at Γ and L valleys have been evaluated and compared with those reported in [64]. Also in this case the agreement is very

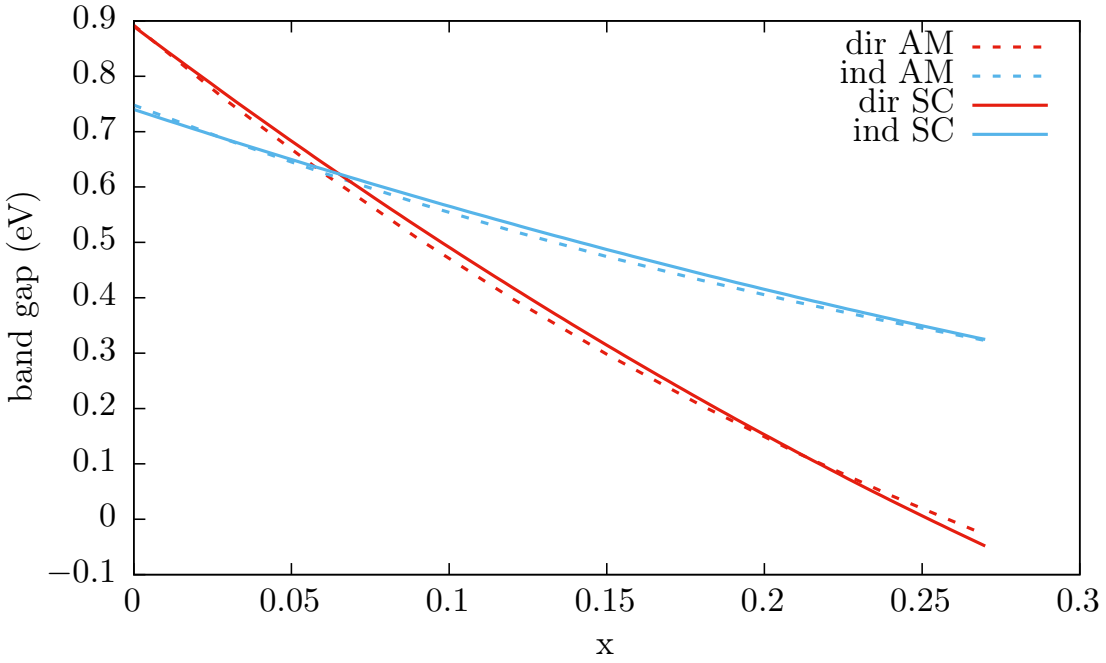

Figure 3.1: Band gaps from AM calculations vs supercell ones taken from [64]; red – direct, blue – indirect.

good which confirms the validity of the method.

To summarize, in this work the computational alchemy approximation has been used to represent the DFT supercell electronic band structure of GeSn alloy with smooth, well fitted curves. The results have been used in [78] to represent the band structure with the 30–bands $\mathbf{k} \cdot \mathbf{p}$ method, suitable in semiconductor device modelling.

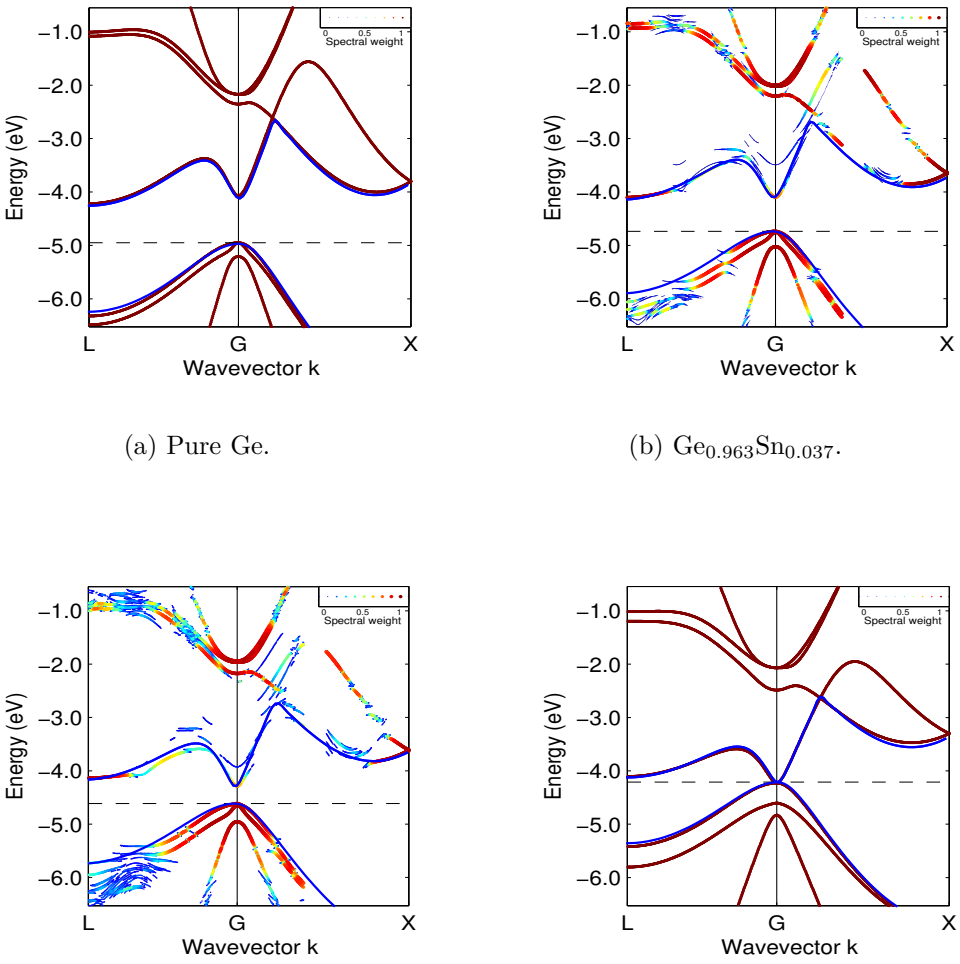

(a) Pure Ge.

(b) $Ge_{0.963}Sn_{0.037}$.

(c) $Ge_{0.87}Sn_{0.13}$.

(d) Pure Sn.

Figure 3.2: AM vs supercell band structures – continuous blue line represents AM results.

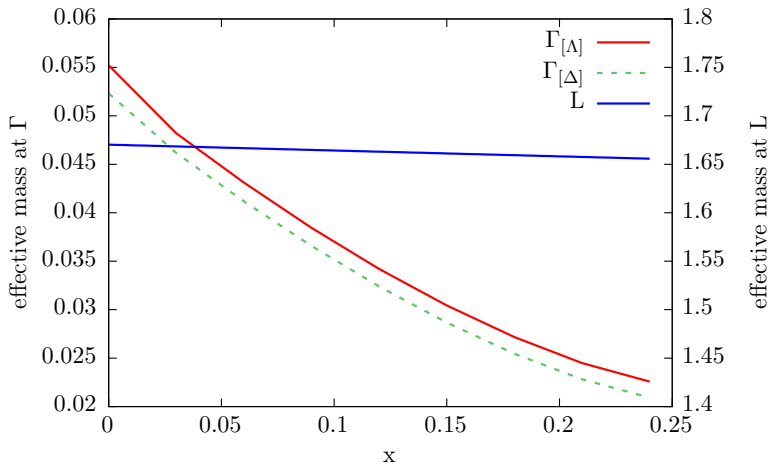

Figure 3.3: Effective masses of electrons in open gap Ge_xSn_{1-x}; red/green – Γ valley, blue – L valley.

Chapter 4

Alternative crystal structures

The third method of electronic structure engineering, mentioned in the introduction, is the formation of alternative (metastable) crystal structures. Modern deposition technologies, like molecular beam epitaxy (MBE) or metal–organic chemical vapor deposition (MOCVD), open such opportunities. Usually the structure is induced by the substrate (e.g. wurtzite structure by the (111) surface of zinc blende crystal). In principle any crystal structure can be formed, but the most important issue is the stability and thermodynamic stability of the system. It is a known fact that the diamond structure is the stable one for Si and Ge, however, for C itself (diamond) is a metastable structure, and although rather difficult to be formed it is a well known system and has various applications, in jewelery in particular, but not only. Diamond owing to its exceptional hardness, very high thermal conductivity (phonon induced), very good electrical insulation properties, transparency for light, has various applications in technics, e.g. diamond anvil cells for creating the high pressure environment. This example shows, that the formation of metastable crystal structures is an open way in the band structure engineering.

In this work only the wurtzite structure will be taken into consideration, since it is energetically very close to the diamond one, and relatively easy to obtain, by deposition on the (111) zinc blende plane. Some properties of such structures of Si and Ge are already known [2, 21–23, 39, 98], in particular it turns out that the fundamental band gap in Ge is direct, (unlike in the diamond structure) which is a crucial feature in optoelectronics. It is worth mentioning that mostly Si was investigated, while Ge barely exists in the literature. The available data range from achievement of Si wurtzite nanowires [23], *ab initio* studies of strained Si, through vibrational [2] and doping properties [21, 22], up to Raman spectrum of Si [39]. Apart from the formation energies, the elastic constants and the Poisson ratio, the systematic investigations of the effect of strains has been performed, for C, Si and Ge. The isotropic (pressure), biaxial (perpendicular to c–axis) and axial (along c–axis) strains have been considered. In particular the effect of strains on the band structure and its crucial features: band gaps (identification of fundamental gaps) and effective masses. Such calculations have allowed also to evaluate the deformation potentials, crucial parameters in the calculations of superstructures electronic bands and of the electron–phonon coupling.

4.1 Computational method

For all of the calculations presented here, VASP [41, 42] software package was used, mainly due to implementation of mBJLDA on PAW pseudopotential. The procedure was similar to the one presented in Chpt. 2. Although, there are a few differences in methodology:

1. The anisotropic strains are considered only with respect to one, [001] axis, which is typical when the structure is grown on (111) ZB substrate. The wurtzite cell is presented in Fig. 4.1.

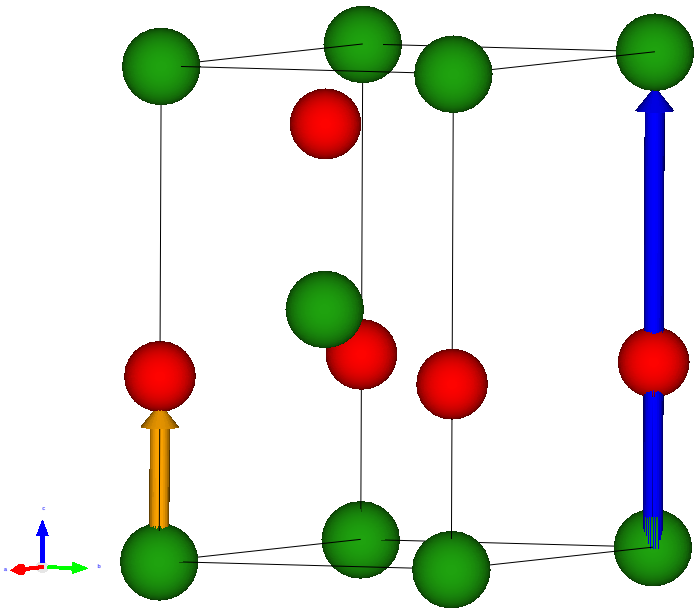

Figure 4.1: Conventional cell of wurtzite (#186).

2. The conventional cell reflects the symmetry of the system, and its possible breaking in the case of anisotropic strains. In wurtzite structure the [001] strains do not lower the symmetry of the cell. What follows the BZ stays the same, and no additional points must be observed. The BZ of wurtzite is shown in Fig. 4.2.

3. The differences in the formation energies between WZ and ZB structures is evaluated, to show the energetic preference. This also gives some hints about stability, especially while straining the system. The thermodynamic stability remains still an open question which require an independent investigations (lattice dynamics).

4. In wurtzite materials two additional values seem to play important role as $\mathbf{k} \cdot \mathbf{p}$ parameters: the Δ_{so} and Δ_{cr}. They are connected to SO coupling and

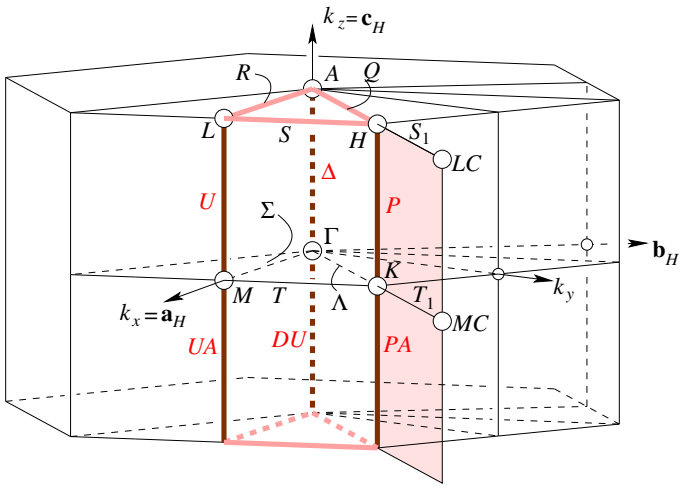

Figure 4.2: First Brillouin Zone of wurtzite crystal structure (#186).

crystal field, and are known to be present in wurtzite crystals, and calculated as follows [6]:

$$\Delta_{so} = \frac{\Delta_1 + \Delta_2}{2} - \frac{1}{2}\frac{c}{a^2} \cdot \sqrt{\Delta} \tag{4.1}$$

$$\Delta_{cr} = \frac{\Delta_1 + \Delta_2}{2} + \frac{1}{2}\frac{c}{a^2} \cdot \sqrt{\Delta} \tag{4.2}$$

where

$$\Delta_1 = HH - LH \tag{4.3}$$

$$\Delta_2 = HH - CH \tag{4.4}$$

$$\Delta = \left(\frac{c}{a^2}\right)^{-2} \cdot (\Delta_1 + \Delta_2)^2 - 4 \cdot \frac{a^2}{c}\Big((\Delta_1 + \Delta_2)^2 - (\Delta_1 - \Delta_2)^2\Big) \tag{4.5}$$

5. Because of different symmetry compared to the diamond one the deformation potentials also differ as well as the way of calculating them. For wurtzite systems (including SO) band structure deformation potential (D_1 to D_6) are

defined by the equations [6]:

$$\begin{aligned}
\Delta E_1 &= E_1 - E_1^0 = (D_1 + D_3)\varepsilon_{zz} + (D_2 + D_4)(\varepsilon_{xx} + \varepsilon_{yy}) + \\
&+ \frac{D_6(E_1^0 - E_2^0 - E_3^0)(\varepsilon_{xz}^2 + \varepsilon_{yz}^2) + D_5 E_1^0[(\varepsilon_{xx} - \varepsilon_{yy})^2 + 4\varepsilon_{xy}^2]}{(E_1^0 - E_2^0)(E_1^0 - E_3^0)}, \qquad (4.6) \\
\Delta E_2 &= E_2 - E_2^0 = (D_1 + D_3\frac{E_2^0}{E_2^0 - E_3^0})\varepsilon_{zz} + \\
&+ (D_2 + D_4\frac{E_2^0}{E_2^0 - E_3^0})(\varepsilon_{xx} + \varepsilon_{yy}) + \frac{E_2^0 E_3^0}{(E_2^0 - E_3^0)^3}(D_3\varepsilon_{zz} + D_4(\varepsilon_{xx} + \varepsilon_{yy}))^2 + \\
&+ \frac{D_6(E_1^0 - E_2^0 + E_3^0)(\varepsilon_{xz}^2 + \varepsilon_{yz}^2) - D_5 E_2^0[(\varepsilon_{xx} - \varepsilon_{yy})^2 + 4\varepsilon_{xy}^2]}{(E_1^0 - E_2^0)(E_2^0 - E_3^0)}, \qquad (4.7) \\
\Delta E_3 &= E_3 - E_3^0 = (D_1 - D_3\frac{E_3^0}{E_2^0 - E_3^0})\varepsilon_{zz} + \\
&+ (D_2 - D_4\frac{E_3^0}{E_2^0 - E_3^0})(\varepsilon_{xx} + \varepsilon_{yy}) - \frac{E_2^0 E_3^0}{(E_2^0 - E_3^0)^3}(D_3\varepsilon_{zz} + D_4(\varepsilon_{xx} + \varepsilon_{yy}))^2 + \\
&+ \frac{D_6(E_1^0 + E_2^0 - E_3^0)(\varepsilon_{xz}^2 + \varepsilon_{yz}^2) - D_5 E_2^0[(\varepsilon_{xx} - \varepsilon_{yy})^2 + 4\varepsilon_{xy}^2]}{(E_1^0 - E_3^0)(E_2^0 - E_3^0)}, \qquad (4.8)
\end{aligned}$$

From Eq. eqs. (4.6) to (4.8) under pure ε_{zz} strain, D_1 and D_2 can be derived, while under planar strains D_3 and D_4. To achieve D_5 and D_6 shear strains are necessary, in particular ε_{xz} or ε_{yz} and ε_{xy}, respectively. The derived deformation potentials are as follows:

$$\begin{aligned}
D_1 &= \frac{1}{\varepsilon_{zz}}(\Delta E_1 + \Delta E_2 + \Delta E_3 - 2\varepsilon_{zz}\Delta E_1) \\
D_2 &= \frac{1}{\varepsilon_{xx} + \varepsilon_{yy}}(\Delta E_1 + \Delta E_2 + \Delta E_3 - 2(\varepsilon_{xx} + \varepsilon_{yy})\Delta E_1) \\
D_3 &= \frac{1}{\varepsilon_{zz}}(\Delta E_2 + \Delta E_3 - 2\varepsilon_{zz}\Delta E_1) \\
D_4 &= \frac{1}{\varepsilon_{xx} + \varepsilon_{yy}}(\Delta E_2 + \Delta E_3 - 2(\varepsilon_{xx} + \varepsilon_{yy})\Delta E_1) \\
D_5 &= \sqrt{\frac{\Delta E_1(E_1^0 - E_2^0)(E_1^0 - E_3^0)}{4E_1^0\varepsilon_{xy}^2}} \\
D_6 &= \sqrt{\frac{\Delta E_1(E_1^0 - E_2^0)(E_1^0 - E_3^0)}{(E_1^0 - E_2^0 - E_3^0)(\varepsilon_{xz}^2 + \varepsilon_{yz}^2)}} \qquad (4.9)
\end{aligned}$$

4.2 Results

4.2.1 Structural and elastic properties

As in the Chapt. 2, the investigations began with achieving parameters of equilibrium wurtzite structures for investigated materials (C, Si and Ge). The symmetry of this type of systems has a unique feature. Some of the atomic sites may flow along c lattice vector direction without changing the symmetry. Thus an additional parameter u is present in the relaxation procedure. In Fig. 4.1 blue arrow represents $\vec{c}$ lattice vector, while orange one represents $u \cdot \vec{c}$. The bulk modulus B_0, it's pressure derivative B_0' and elastic constants (from c_{11} to c_{33}) were also evaluated.

Table 4.1: Elastic parameters.

	C	Si	Si–ref [71]	Ge
a (Å)	2.498	3.823	3.828	4.005
c (Å)	4.159	6.323	6.325	6.594
u	0.374	0.374	0.374	0.375
B_0 (GPa)	450	94	92.8	67
B_0'	3.65	4.57	4.24	4.71
c_{11} (GPa)	1219	187	237 - c_{12}	125
c_{12} (GPa)	106	54	237 - c_{11}	54
c_{13} (GPa)	19	38	317	22
c_{33} (GPa)	1332	213	313	162

The only reference data found in the literature are for Si [71]. Very satisfactory agreement of these data with those obtained in this work can be seen (see Tab. 4.1). The lattice constants differ on third decimal point, while the bulk modulus and the elastic constants differ no more than 10 GPa.

In Tab. 4.2 the pressure related to isotropic strain is presented in the form of the linear (b) and the quadratic (a) coefficients.

Table 4.2: Pressure coefficients.

	C	Si	Ge
a (GPa)	-0.79	-0.19	-0.14
b (GPa)	13.45	2.81	2.00

The Poisson ratios, both for uniaxial and biaxial strains are shown in Tab. 4.3.

The formation energies as functions of strain are presented in Fig. 4.3

Because of the lack of experimental data, the elastic properties are compared with those of the zinc blend ones. Despite the change in the structure, the chemical trends are preserved. Both the elastic constants and the bulk modulus are very

Table 4.3: Poisson's ratios (ν) for axial (type 1) and biaxial (type 2) strains.

material	1	2
C	0.02	0.03
Si	0.16	0.38
Ge	0.13	0.29
Sn	0.18	0.44

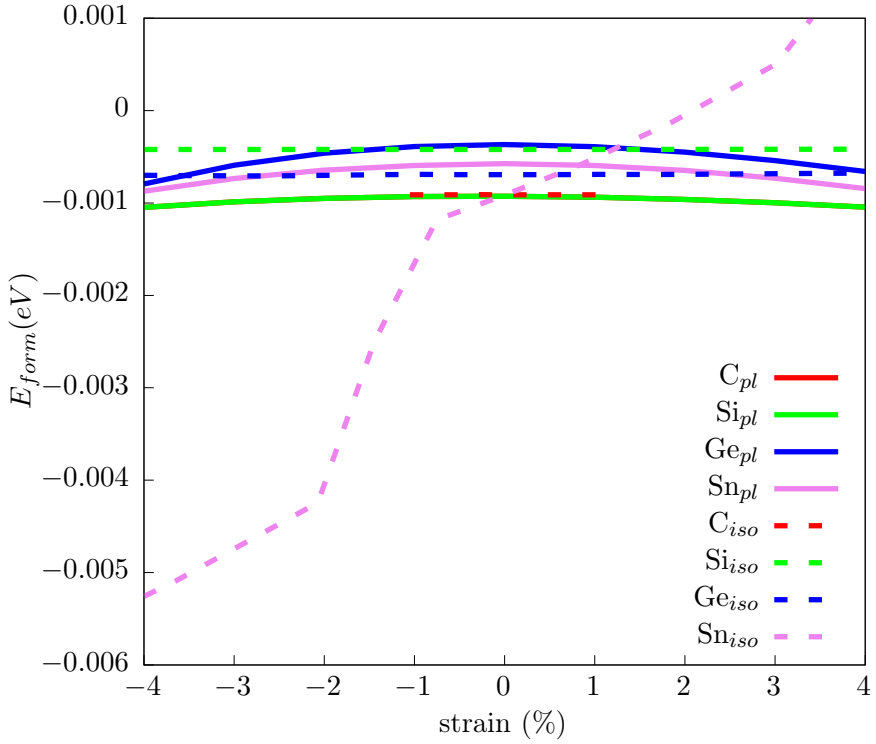

Figure 4.3: Formation energy of group IV materials (calculated as energy per atom in zinc blend minus wurtzite). *pl* stands for planar strains in zinc blend (111) and wurtzite (001), while *iso* stands for isotropic strains for both systems.

high for C and decrease while moving downward the periodic table. The related to isotropic strains hydrostatic pressure also shows the toughness of diamond. As in zinc blend structure, wurtzite systems show slight non–linear behaviour of pressure induced by strain. Calculated Poisson's ratios shows similar behavior to the zinc blende ones. At biaxial strains they are bigger than at axial ones, and the more massive atom the higher is the value (with exception of Ge, which has lower value than for Si). On the contrary, the ratios do not exceed 0.5, even in biaxial cases.

The analysis of the formation energy as dependent on strain shows that only Sn seems to energetically prefer the wurtzite structure, under tensile isotropic strain. In every other case, preferable is the zinc blend structure. Moreover, the more strained system (no matter compressive or tensile) the more energetically preferable is the zinc blend over wurtzite structure. On the other hand, the value of difference of

energy per atom is rather small (excluding isotropic Sn, below $-0.001\ eV$) which means that the energetic criterion is of a lower meaning in determination of system preferences.

4.2.2 Electronic structure

The second part of the results concern the electronic structure properties. As in Chpt. 2, the main focus is given to strain effects. In the first step the electronic band structures along paths containing high symmetry directions have been evaluated. This allowed us to the find direct and the indirect gaps and, what is of crucial meaning, to identify the fundamental gaps. In the following steps the effective masses at band extrema have been evaluated and finally the deformation potentials. Table 4.4 shows the basic parameters at equilibrium state along with deformation potentials for each of the investigated materials.

Table 4.4: Electronic band structure parameters.

	C	Si	Ge
E_g^{Γ} (eV)	6.517	1.649	0.362
E_g^{M} (eV)	5.800	1.015	0.897
E_g^{K} (eV)	5.318	1.471	1.879
Δ_{so} (eV)	0.011	0.048	0.272
Δ_{cr} (eV)	0.516	0.351	0.251
D_1	0.43	5.38	0.34
D_2	0.50	0.46	-0.07
D_3	0.16	3.59	0.19
D_4	0.225	0.24	1.31
D_5	0.275	1.18	1.1
D_6	0.24	0.27	0.64

There is no reference data for the deformation potentials but they seem to have reasonable values. The method itself for calculating the deformation potentials is precisely described and have strong physical foundations as well as the parameters used for *ab initio* calculations were rigid.

The table above 4.4 shows in particular the gaps for Ge, which proves that there is a direct band gap at equilibrium state. As for the other materials, the indirect band gap prevails but certain perspective still exists that under the strain the situation may change in favour of the direct band gap. To observe this, the fundamental band gaps under strain are presented (Fig. 4.4a along with effective masses of carriers (Fig. 4.4b) at Γ k–point (for holes) and at fundamental gap k–point (for electrons). Both in Δ and Λ directions.

In Fig. 4.4a one can see that in the case of Ge the direct band gap appears at almost all applied strains. Only at biaxial compressive strain higher than 2%, the gap is indirect. Moreover, the value of the direct gap may vary from actually closed one (at biaxial tensile and axial compressive strain) to even more than 0.6 eV (in

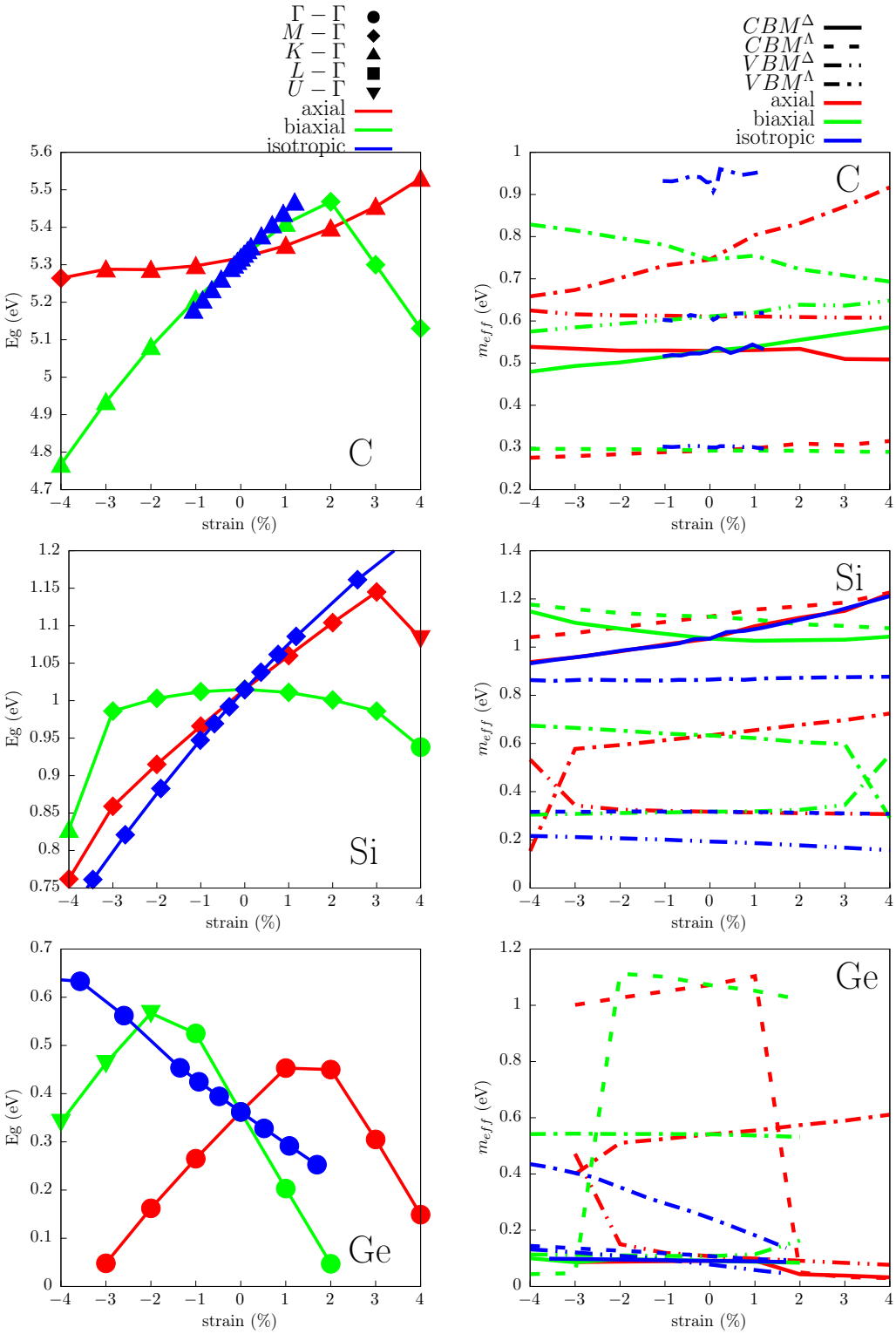

(a) Fundamental band gaps.

(b) Effective mass of charge carriers.

Figure 4.4: Band structure parameters in wurtzite system group IV materials.

isotropic compressive strain). This fact together with the fact that the effective masses of electrons and holes in Δ direction are below 0.2 m_e, opens interesting perspectives for applications of this material in infrared optoelectronics. Apart from Ge, only Si appears to have direct band gap under biaxial tensile strain, but only above 4%, which is a quite high value.

The data obtained in this work for Si can be compared with the literature data [71], which are also theoretical. The lattice constants differ on second decimal point and the fundamental band gap value differs around 0.2 eV, although the type of gap is the same ($\Gamma - M$). The equilibrium state band gaps are almost the same. The transitions of type of fundamental gap is exactly at the same strain value for all three straining types. The difference can be seen in the slope of band gap changes, in presented results it is slightly lower and in biaxial strains the parabolic behaviour is more distinct, unlike in the reference. Nevertheless, the agreement is good enough to enhance the credibility of the rest of the investigated materials.

For the full picture Δ_{so} and Δ_{cr} were also calculated for all the types of strains and their range. The results are shown in the Fig. 4.5.

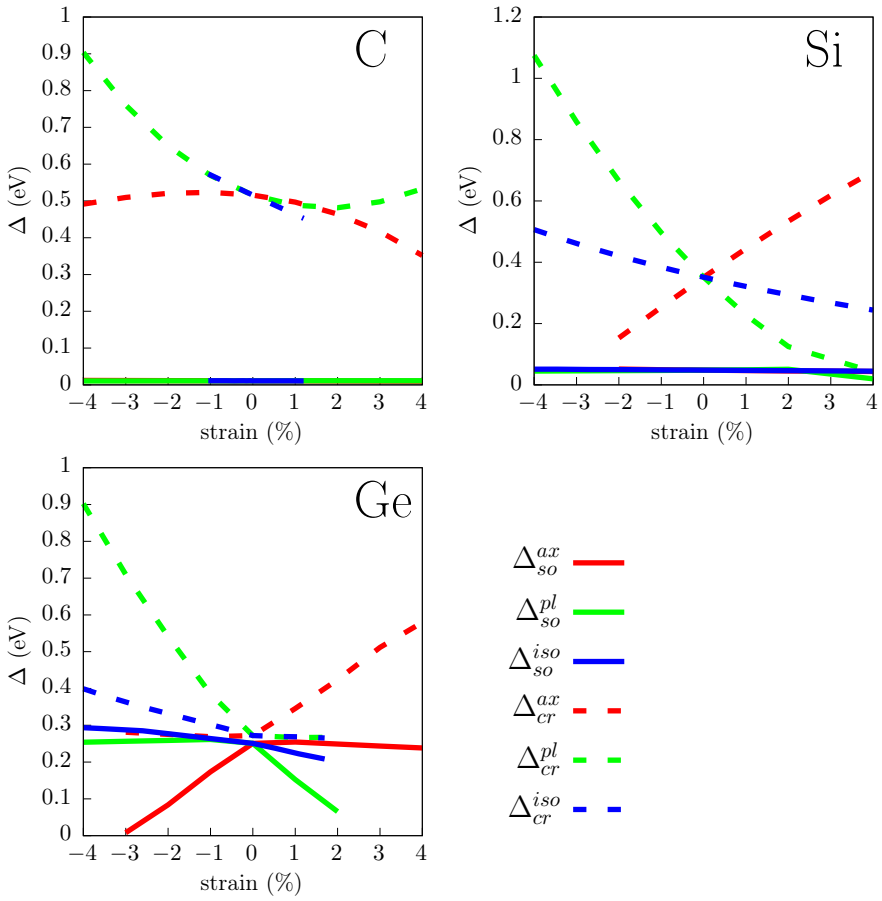

Figure 4.5: Strain dependence of Δ_{so} and Δ_{cr} in wurtzite group IV systems.

While there are almost no changes in the Δ_{so} parameters, the Δ_{cr} vary significantly, up to 4-times in Ge at biaxial strain.

Chapter 5

Spacial Confinement

The last method of electronic structure engineering listed in the introduction is the spatial confinement. This is a well known method which consists in formation of various nano–structures (quantum dots, superstructures, etc.), where some additional built-in potential (apart from crystal cell periodic) emerges [54, 82]. E.g. in superstructures, which are systems of semiconductor layers, the quantum wells are formed where a spacial confinement leads to shifts of energy levels present in the bulk systems or creation of new levels. Similarly in quantum dots, where the external confining potential (often modeled as a parabolic one) leads to localisation of carriers whose basic properties are determined by the bulk crystal structure of the material the quantum dot is formed of.

In this work the idea of a digital alloy is exploited. The digital alloy, is a mixed system of 2 or more semiconductors, but at variance with random alloy they are mixed in ordered way, most often in the form of layered system (e.g. [53]). Formation of such systems is possible owing to modern epitaxial technologies, and the advantage is that the structural parameters are well determined whereas in random alloys there is always a question about the level of randomness, the effect of components segregation etc. The random alloys in modeling are usually assumed to be perfectly random, which in *ab initio* calculations is emulated in terms of supercells, the special quasirandom structure (SQS) technique and the following unfolding procedure approach which leads to the spectral character of the band structure (at each k-point there is certain energy spectrum instead of discrete energy levels). In the case of the digital alloy there is no such problem. Although the supercells must still be used, they form an ordered structure which reflects the real situation. The supercell becomes an elementary cell which has additional implications, namely the indirect gap may become a direct one simply by the folding effect and the energy spectrum at each k-point remains discrete.

In this work the digital alloy of Si–Ge is considered. Both semiconductors in the bulk form exhibit indirect fundamental band gap. However, the formation of an ordered layered system leads to a new crystal structure and corresponding BZ in such a way that the indirect band gap can be folded into the direct one. Moreover, the layered system is always formed on some substrate and an additional strain is induced which leads to the modification of the component material band structure, as it was shown in Chpt. 2. Those two facts (the band structure folding and strains) lead to unpredictable features of the band structure of a digital alloy,

whose knowledge requires dedicated investigations. To my best knowledge the idea presented in this chapter is original, i.e. no such investigations has been reported in the literature so far. The only found Si or Ge digital alloy systems are the ones layered with Mn to achieve magnetic ordering [15, 57, 58].

5.1 Computational method

Digital alloys can be formed e.g. by molecular beam epitaxy method which means that the substrate determines the in–plane lattice constants. The calculations presented in this work have a preliminary character and are limited to (100) surface, pure Si and Ge as substrates and 2-layer systems SiSiGeGe. However, the investigations will be continued with bigger number of layers per material and also for (111) plane. The bigger number of layers per material makes Brillouin Zone and the band folding different, thus may have a strong impact on the band structure. Similarly the choice of (111) plane results in the folding in other direction than in the case of (100) plane. This means that both the number of layers per material and the digital alloy formation direction may have a crucial meaning for the electronic band structure.

As a preliminary outlook both (100) and (111) structures are visualized. The elementary cells were drawn and presented in Figs. 5.1a and 5.1b.

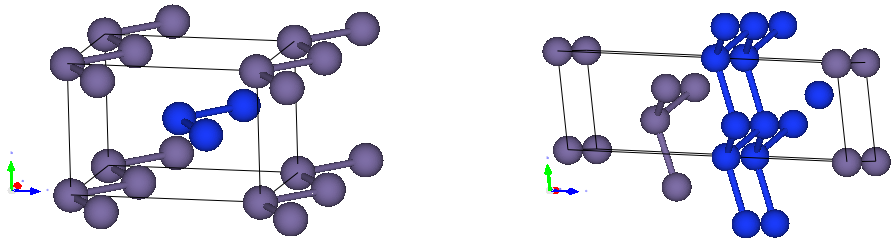

(a) [100] direction. (b) [111] direction.

Figure 5.1: Conventional cell of digital alloys structures.

Also the BZ for those structures are presented to analyze which points and paths should be considered during electronic calculations. The BZ were drawn from VASP POSCAR files using online tool *SeeK-path*. The BZ are illustrated in Fig. 5.2a and 5.2b.

Due to the fact that here one must work with bigger systems (relaxation procedure of volume shape and atomic positions) and it might require significant amount of computational resources, a test was performed whether it is possible to use Poisson's ratio, calculated in 2 instead of relaxing each of the investigated systems. For 2 atomic layers per material systems, the test results showed that the use of Poisson's ratio sufficiently represents the atomic structure, which significantly reduces the computational effort and can be applied for bigger systems.

After that the electronic calculations were performed. The most desirable result from digital alloys investigation is the change of fundamental band gap while moving

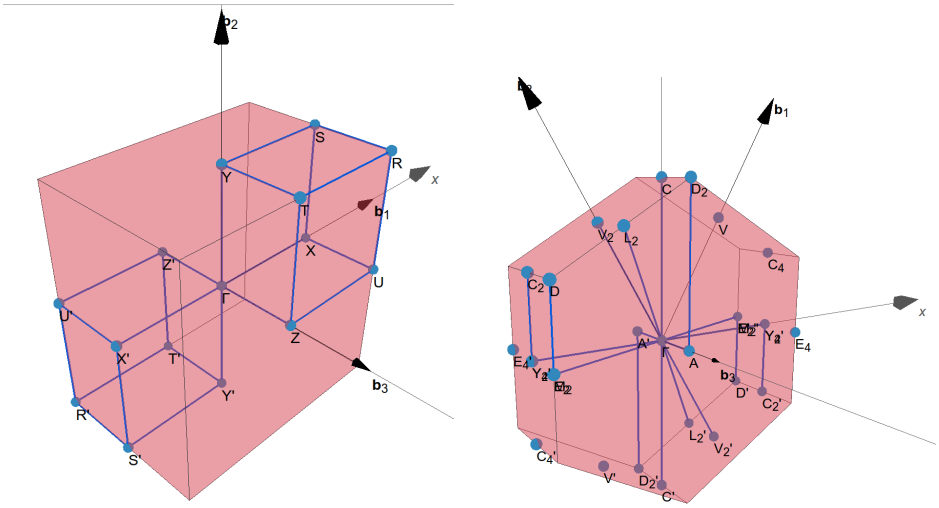

(a) [100] direction. (b) [111] direction.

Figure 5.2: BZ of digital alloys structures.

through the layers in the growth direction. To be able to analyse it, this was necessary to use VASP code, due to the fact that it has mBJLDA implemented (which gives accurate band gaps) along with PAW which allows for orbital decomposition (so–called *fatbands*). Also DOS can be decomposed for each atom separately which may be beneficial for more precise band gap changes evaluation.

All of the testing calculations were performed using ABINIT software package with PAW–LDA combination, while electronic calculations with VASP code along with mBJLDA exchange–correlation functional.

5.2 Results

In the beginning, Poisson's ratio test results were evaluated. The difference of atomic positions and lattice vectors between relaxation procedure and Poisson's ratio on testing structures prove to be on the fourth decimal point or below. This is sufficient enough to use Poisson's ratio and atomic position of previous calculations instead of relaxation procedure. It should be stated here that this was possible only due to the usage of the same XC functional and pseudopotential as it was practiced in the investigations of the strain effects (Chpt. 2).

5.2.1 Band structure

Although the bulk crystal structures of the component materials are the the diamond ones, due to layered nature, the BZ of the system differs (as it has been explained above). It is not known to which points the focus should be given so the path was chosen to cover all of the characteristic points and to be the most representative. For the [100] direction the path was set to $Y - \Gamma - X - U - Z - \Gamma$.

The crucial criterium was to cover both in–plane and along crystal growth directions to analyze how the electrons will behave in both directions.

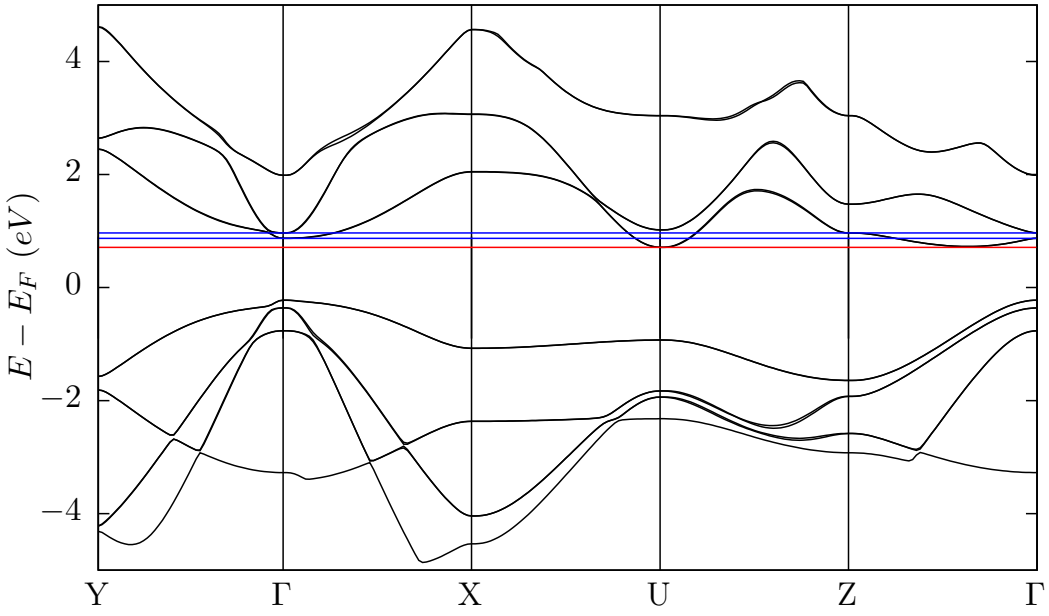

(a) Band structure.

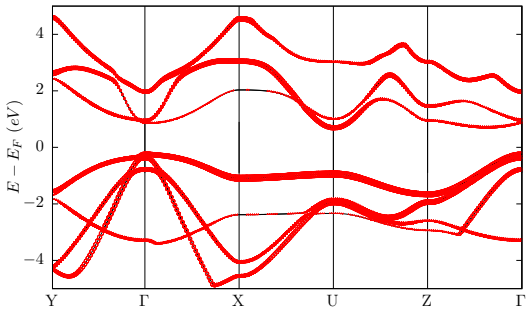

(b) Ge_1

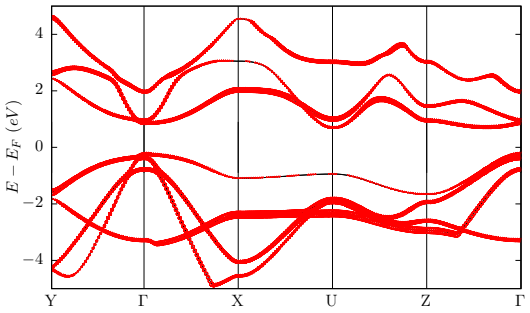

(c) Ge_2

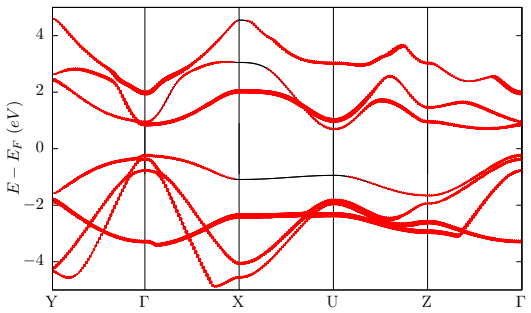

(d) Si_1

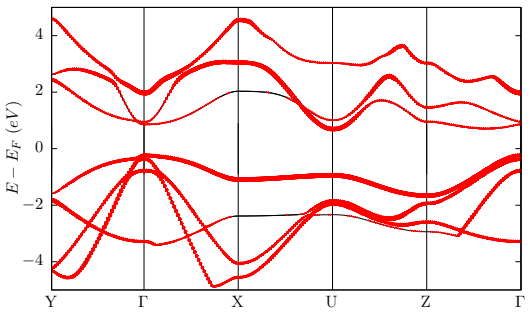

(e) Si_2

Figure 5.3: Atomic decomposition of band structure of [100] direction on Si substrate.

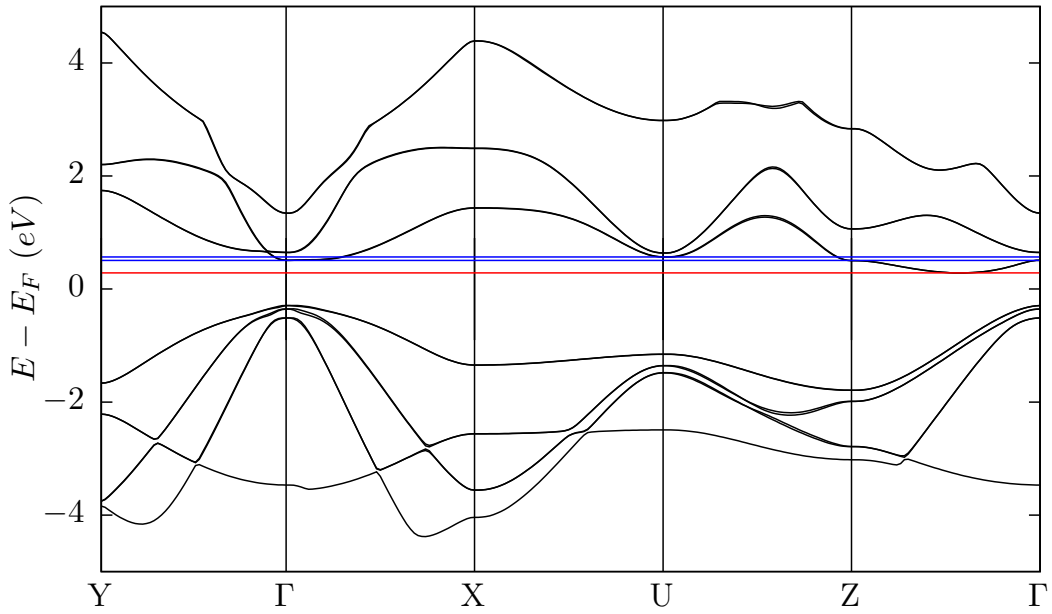

(a) Band structure.

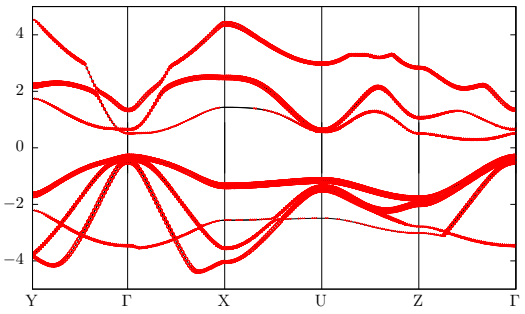

(b) Ge_1

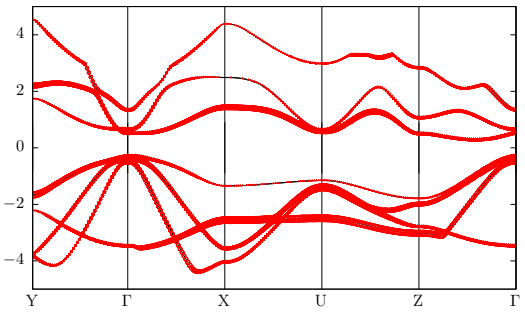

(c) Ge_2

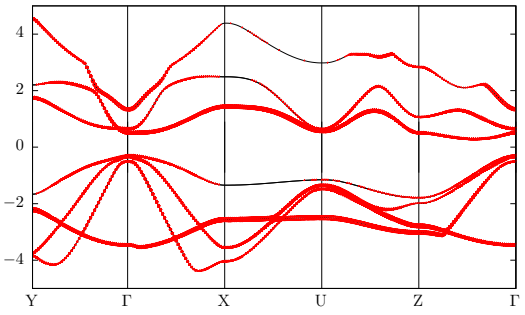

(d) Si_1

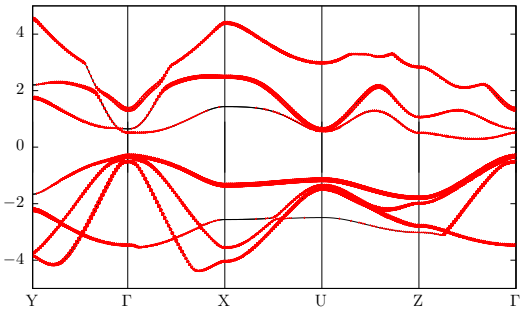

(e) Si_2

Figure 5.4: Atomic decomposition of band structure of [100] direction on Ge substrate.

As a preliminary results, in Figs. 5.3 and 5.4 the band structures are shown for the cases of (100) plane and Si and Ge substrates, together with the decomposition for each atom in elementary cell. Some interesting features of the band structures can be observed. In both systems the direct gap of the order of $1eV$ can be observed, which is presumably a result of Si Γ-X band folding. However, in the case of Si substrate, the fundamental gap seems to be indirect, from Γ point to U point, but the situation looks different when looking at the atom projected band structures. Here, considering the Ge2 and Si1 atoms, the band gap is direct. Moreover, the $X - U$ direction is perpendicular to the layered system, and a question arises about spatial distribution of band gap energies in the direction perpendicular to the layered systems. Here, a kind of quantum well system can be expected, which can be studied by evaluating the spatially resolved band gaps, for the vertical direction. In the case of Ge substrate the band gap is direct around Γ, is smaller than $1eV$, and in the direction $\Gamma - Z$ (perpendicular to the layers) has a nesting character, wheres at U point the bands at CB minimum are degenerate.

The presented results show that the idea of the Ge-Si digital alloy is promising and deserves further attention. Some interesting features of electronic band structures have been demonstrated here, leading to important questions which should be addressed: 1. what is the effect of increasing number of a given material layers, 2. how the band structures will look like for (111) direction, 3. how the spatially resolved band gaps (in the vertical direction) behave, and what are the consequences of this behavior for optical properties, 4. what are the oscillator strengths of identified possible optical transitions, and how they, together with the energetic structure affect the optical response. Another intriguing perspective is an extension of the investigations on the Ge-Si digital alloys in wurtzite structures, discussed in Chpt. 4, where germanium exhibits already a direct fundamental gap, independently of strains, and the role silicon should be determined. Here, the c-direction seems to be natural to form such an alloy, and the band folding in this direction can introduce unpredicted effects. All those issues will be a subject of the planned further investigations

Chapter 6

Summary

This disertation is devoted to the band structure engineering of group IV atomic systems. Of particular interest are well known semiconductors Si, Ge and also Sn which itself can be semiconducting at special external conditions (strain) or when admixed to Ge or Si can modify their properties. For consistency purposes also carbon has been included in investigations. This work, on the one hand, contains a rich collection of results which pretend to be systematic and in many cases original, but on the other hand it is a kind of review of possible methods in the band structure engineering. Four methods have been distinguished: strains, alloying, structural changes and quantum confinement. Strains (Chpt. 2), when applied, lead to a significant modification of the electronic structure, band gaps, and effective masses. All those features have crucial meaning in applications. Strains are also accessible in technologies, mainly via substrate induced strains, but also via chemical pressure, when large grains of a material are surrounded by another material in a coherent crystal lattice having certain intermediate crystal parameters. Alloying (Chpt. 3), as it has been demonstrated on the example of the GeSn system, is a very promissing method, which in particular leads to the indirect–direct band transition. Various concepts appear in this context, like formation of ternary and quaternary alloys, including strains, not isovalent doping, etc. The formation of alternative crystal structures (Chpt. 4) is a method relatively less exploited, perhaps because of technological difficulties. However, it is a known fact that such systems exist and are known to have properties needed in applications, like eg. Ge in wurtzite structure, exhibiting not only direct band gaps but also low effective messes. Finally, the quantum confinement (Chpt. 5) is realized e.g. in quantum dots or superstructures. In this case and additional "external" (although built-in) potential is present in the system and in the resulting quantum wells some quantum levels appear which, when superimposed with the crystal electronic structure, lead to a significant modification of the electronic structure. In this work an idea of the Si–Ge digital alloy is introduced, which to the author best knowledge has never been exploited so far. Here, only some preliminary results are presented, but the obtained band structures and orbital compositions are very promising, and prove that the idea should be subjected to further detailed investigations.

To summarize, this work forms a rich, systematic, consistent report on various methods of electronic structure modification, on the example of the group IV elements. A lot of results are original and other are compared and verified with the

literature data, which enhances the credibility of the reported computational work. An open way for further and very promising investigations is also defined.

A lot of results from Chpts. 4 and 5 are original and will be a subject of publications in the nearest future.

Acknowledgements

The calculations conducted for this work were performed in: Wroclaw Center for Networking and Computing and Academic Computer Centre Cyfronet AGH.

Bibliography

1. P. Aella, C. Cook, J. Tolle, S. Zollner, A. V. G. Chizmeshya, J. Kouvetakis, *Applied Physics Letters* **84**, 888–890, eprint: https://doi.org/10.1063/1.1645324 (2004).
2. J. Bandet, B. Despax, M. Caumont, *Journal of Physics D: Applied Physics* **35**, 234–239 (2002).
3. M. Bauer, J. Taraci, J. Tolle, A. V. G. Chizmeshya, S. Zollner, D. J. Smith, J. Menendez, C. Hu, J. Kouvetakis, *Applied Physics Letters* **81**, 2992–2994, eprint: https://doi.org/10.1063/1.1515133 (2002).
4. L. Bellaiche, D. Vanderbilt, *Phys. Rev. B* **61**, 7877–7882 (12 2000).
5. L. Bellaiche, D. Vanderbilt, *Phys. Rev. B* **61**, 7877–7882 (12 2000).
6. G. Bir, G. Pikus, "Symmetry and Strain-induced Effects in Semiconductors", (Wiley, 1974).
7. A. Blacha, H. Presting, M. Cardona, *physica status solidi (b)* **126**, 11–36, eprint: https://onlinelibrary.wiley.com/doi/pdf/10.1002/pssb.2221260102 (1984).
8. P. E. Blöchl, *Phys. Rev. B* **50**, 17953–17979 (24 1994).
9. T. B. Boykin, G. Klimeck, F. Oyafuso, *Phys. Rev. B* **69**, 115201 (11 2004).
10. T. Brudevoll, D. S. Citrin, N. E. Christensen, M. Cardona, *Phys. Rev. B* **48**, 17128–17137 (23 1993).
11. J. A. Camargo-Martınez, R. Baquero, *Phys. Rev. B* **86**, 195106 (19 2012).
12. Y. Chibane, M. Ferhat, *Journal of Applied Physics* **107**, 053512–053512 (2010).
13. A. V. G. Chizmeshya, M. R. Bauer, J. Kouvetakis, *Chemistry of Materials* **15**, 2511–2519, eprint: https://doi.org/10.1021/cm0300011 (2003).
14. J. Chrétien, N. Pauc, F. Armand Pilon, M. Bertrand, Q.-M. Thai, L. Casiez, N. Bernier, H. Dansas, P. Gergaud, E. Delamadeleine, R. Khazaka, H. Sigg, J. Faist, A. Chelnokov, V. Reboud, J.-M. Hartmann, V. Calvo, *ACS Photonics* **6**, 2462–2469, eprint: https://doi.org/10.1021/acsphotonics.9b00712 (2019).
15. A. Continenza, F. Antoniella, S. Picozzi, *Phys. Rev. B* **70**, 035310 (3 2004).
16. V. R. D'Costa, C. S. Cook, A. G. Birdwell, C. L. Littler, M. Canonico, S. Zollner, J. Kouvetakis, J. Menéndez, *Phys. Rev. B* **73**, 125207 (12 2006).

17. S. de Gironcoli, P. Giannozzi, S. Baroni, *Phys. Rev. Lett.* **66**, 2116–2119 (16 1991).

18. C. Eckhardt, K. Hummer, G. Kresse, *Phys. Rev. B* **89**, 165201 (16 2014).

19. M. El Kurdi, G. Fishman, S. Sauvage, P. Boucaud, *Journal of Applied Physics* **107**, 013710, eprint: `https://doi.org/10.1063/1.3279307` (2010).

20. B. Elias, *Advances in Physics Theories and Applications* **25**, 82–91 (2013).

21. F. Fabbri, E. Rotunno, L. Lazzarini, D. Cavalcoli, A. Castaldini, N. Fukata, K. Sato, G. Salviati, A. Cavallini, *Nano Letters* **13**, PMID: 24224918, 5900–5906, eprint: `https://doi.org/10.1021/nl4028445` (2013).

22. F. Fabbri, E. Rotunno, L. Lazzarini, N. Fukata, G. Salviati, *Scientific Reports* **4**, 3603 (2014).

23. A. Fontcuberta i Morral, J. Arbiol, J. D. Prades, A. Cirera, J. R. Morante, *Advanced Materials* **19**, 1347–1351, eprint: `https://onlinelibrary.wiley.com/doi/pdf/10.1002/adma.200602318` (2007).

24. M. Gladysiewicz, R. Kudrawiec, M. S. Wartak, *IEEE Journal of Quantum Electronics* **50**, 1–10 (2014).

25. M. Gladysiewicz-Kudrawiec, R. Kudrawiec, J. Miloszewski, P. Weetman, J. Misiewicz, M. Wartak, *Journal of Applied Physics* **113** (2013).

26. B. Gonzalez, V. Palankovski, H. Kosina, A. Hernandez, S. Selberherr, *Solid-State Electronics* **43**, 1791–1795 (1999).

27. X. Gonze, B. Amadon, P.-M. Anglade, J.-M. Beuken, F. Bottin, P. Boulanger, F. Bruneval, D. Caliste, R. Caracas, M. Côté, T. Deutsch, L. Genovese, P. Ghosez, M. Giantomassi, S. Goedecker, D. Hamann, P. Hermet, F. Jollet, G. Jomard, S. Leroux, M. Mancini, S. Mazevet, M. Oliveira, G. Onida, Y. Pouillon, T. Rangel, G.-M. Rignanese, D. Sangalli, R. Shaltaf, M. Torrent, M. Verstraete, G. Zerah, J. Zwanziger, *Computer Physics Communications* **180**, 40 YEARS OF CPC: A celebratory issue focused on quality software for high performance, grid and novel computing architectures, 2582–2615 (2009).

28. X. Gonze, F. Jollet, F. A. Araujo, D. Adams, B. Amadon, T. Applencourt, C. Audouze, J.-M. Beuken, J. Bieder, A. Bokhanchuk, E. Bousquet, F. Bruneval, D. Caliste, M. Côté, F. Dahm, F. D. Pieve, M. Delaveau, M. D. Gennaro, B. Dorado, C. Espejo, G. Geneste, L. Genovese, A. Gerossier, M. Giantomassi, Y. Gillet, D. Hamann, L. He, G. Jomard, J. L. Janssen, S. L. Roux, A. Levitt, A. Lherbier, F. Liu, I. Lukačević, A. Martin, C. Martins, M. Oliveira, S. Poncé, Y. Pouillon, T. Rangel, G.-M. Rignanese, A. Romero, B. Rousseau, O. Rubel, A. Shukri, M. Stankovski, M. Torrent, M. V. Setten, B. V. Troeye, M. Verstraete, D. Waroquiers, J. Wiktor, B. Xu, A. Zhou, J. Zwanziger, *Computer Physics Communications* **205**, 106–131 (2016).

29. K. Guilloy, N. Pauc, A. Gassenq, J. Escalante Fernandez, I. Duchemin, Y.-M. Niquet, S. Tardif, G. Osvaldo Dias, D. Rouchon, J. Widiez, J.-M. Hartmann, R. Geiger, T. Zabel, H. Sigg, J. Faist, A. Chelnokov, V. Reboud, V. Calvo, *ACS Photonics* **3**, 1907 (2016).

30. P. Haas, F. Tran, P. Blaha, *Phys. Rev. B* **79**, 085104 (8 2009).

31. G. He, H. A. Atwater, *Phys. Rev. Lett.* **79**, 1937–1940 (10 1997).

32. Y. Hinuma, A. Grüneis, G. Kresse, F. Oba, *Phys. Rev. B* **90**, 155405 (15 2014).

33. P. Hohenberg, W. Kohn, *Phys. Rev.* **136**, B864–B871 (3B 1964).

34. K. Homewood, M. Lourenço, *Nature Photon.* **9**, 78–79 (2015).

35. W. Huang, B. Cheng, C. Xue, C. Li, *Physica B: Condensed Matter* **443**, 43–48 (2014).

36. H. Jalili, J. W. Han, Y. Kuru, Z. Cai, B. Yildiz, *The Journal of Physical Chemistry Letters* **2**, 801–807, eprint: `https://doi.org/10.1021/jz200160b` (2011).

37. N. Janik, P. Scharoch, R. Kudrawiec, *Computational Materials Science* **181**, 109729 (2020).

38. Y.-S. Kim, M. Marsman, G. Kresse, F. Tran, P. Blaha, *Phys. Rev. B* **82**, 205212 (20 2010).

39. R. J. Kobliska, S. A. Solin, *Phys. Rev. B* **8**, 3799–3802 (8 1973).

40. W. Kohn, L. J. Sham, *Phys. Rev.* **140**, A1133–A1138 (4A 1965).

41. G. Kresse, J. Furthmüller, *Computational Materials Science* **6**, 15–50 (1996).

42. G. Kresse, J. Furthmüller, *Phys. Rev. B* **54**, 11169–11186 (16 1996).

43. H. P. Ladrón de Guevara, A. G. Rodríguez, H. Navarro-Contreras, M. A. Vidal, *Applied Physics Letters* **84**, 4532–4534, eprint: `https://doi.org/10.1063/1.1758772` (2004).

44. M.-H. Lee, P.-L. Liu, Y.-A. Hong, Y.-T. Chou, J.-Y. Hong, Y.-J. Siao, *Journal of Applied Physics* **113**, 063517, eprint: `https://doi.org/10.1063/1.4790362` (2013).

45. K. Lejaeghere, G. Bihlmayer, T. Björkman, P. Blaha, S. Blügel, V. Blum, D. Caliste, I. E. Castelli, S. J. Clark, A. Dal Corso, S. de Gironcoli, T. Deutsch, J. K. Dewhurst, I. Di Marco, C. Draxl, M. Dułak, O. Eriksson, J. A. Flores-Livas, K. F. Garrity, L. Genovese, P. Giannozzi, M. Giantomassi, S. Goedecker, X. Gonze, O. Grånäs, E. K. U. Gross, A. Gulans, F. Gygi, D. R. Hamann, P. J. Hasnip, N. A. W. Holzwarth, D. Iuşan, D. B. Jochym, F. Jollet, D. Jones, G. Kresse, K. Koepernik, E. Küçükbenli, Y. O. Kvashnin, I. L. M. Locht, S. Lubeck, M. Marsman, N. Marzari, U. Nitzsche, L. Nordström, T. Ozaki, L. Paulatto, C. J. Pickard, W. Poelmans, M. I. J. Probert, K. Refson, M. Richter, G.-M. Rignanese, S. Saha, M. Scheffler, M. Schlipf, K. Schwarz, S.

Sharma, F. Tavazza, P. Thunström, A. Tkatchenko, M. Torrent, D. Vanderbilt, M. J. van Setten, V. Van Speybroeck, J. M. Wills, J. R. Yates, G.-X. Zhang, S. Cottenier, *Science* **351**, eprint: https://science.sciencemag.org/content/351/6280/aad3000.full.pdf (2016).

46. H. S. Mączko, R. Kudrawiec, M. Gladysiewicz, *Sci. Rep.* **9**, 3316 (2019).

47. J. Margetis, S. Al-Kabi, W. Du, W. Dou, Y. Zhou, T. Pham, P. Grant, S. Ghetmiri, A. Mosleh, B. Li, J. Liu, G. Sun, R. Soref, J. Tolle, M. Mortazavi, S.-Q. Yu, *ACS Photonics* **5**, 827–833, eprint: https://doi.org/10.1021/acsphotonics.7b00938 (2018).

48. M. A. Marques, M. J. Oliveira, T. Burnus, *Computer Physics Communications* **183**, 2272–2281 (2012).

49. N. Marzari, S. de Gironcoli, S. Baroni, *Phys. Rev. Lett.* **72**, 4001–4004 (25 1994).

50. H. J. Monkhorst, J. D. Pack, *Phys. Rev. B* **13**, 5188–5192 (12 1976).

51. P. Moontragoon, Z. Ikonić, P. Harrison, *Semiconductor Science and Technology* **22**, 742–748 (2007).

52. S. J. Murray, M. A. Marioni, A. M. Kukla, J. Robinson, R. C. O'Handley, S. M. Allen, *Journal of Applied Physics* **87**, 5774–5776, eprint: https://doi.org/10.1063/1.372518 (2000).

53. P. G. Newman, J. Pamulapati, H. Shen, M. Taysing-Lara, J. Liu, W. Chang, G. Simonis, B. Koley, M. Dagenais, S. Feld, J. Loehr, *Journal of Vacuum Science & Technology B: Microelectronics and Nanometer Structures Processing, Measurement, and Phenomena* **18**, 1619–1622, eprint: https://avs.scitation.org/doi/pdf/10.1116/1.591439 (2000).

54. S. A. Nikishin, M. Holtz, H. Temkin, *Japanese Journal of Applied Physics* **44**, 7221–7226 (2005).

55. Y.-M. Niquet, D. Rideau, C. Tavernier, H. Jaouen, X. Blase, *Physical Review B* **79**, 245201 (2009).

56. http://www.ioffe.ru/SVA/NSM/Semicond/, Accessed: 2021-04-09.

57. M. M. Otrokov, A. Ernst, S. Ostanin, G. Fischer, P. Buczek, L. M. Sandratskii, W. Hergert, I. Mertig, V. M. Kuznetsov, E. V. Chulkov, *Phys. Rev. B* **83**, 155203 (15 2011).

58. M. M. Otrokov, A. Ernst, V. V. Tugushev, S. Ostanin, P. Buczek, L. M. Sandratskii, G. Fischer, W. Hergert, I. Mertig, V. M. Kuznetsov, E. V. Chulkov, *Phys. Rev. B* **84**, 144431 (14 2011).

59. R. Pandey, M. Rérat, M. Causà, *Applied Physics Letters* **75**, 4127–4129, eprint: https://doi.org/10.1063/1.125558 (1999).

60. J. P. Perdew, Y. Wang, *Phys. Rev. B* **45**, 13244–13249 (23 1992).

61. J. P. Perdew, Y. Wang, *Phys. Rev. B* **45**, 13244–13249 (23 1992).

62. M. P. Polak, P. Scharoch, R. Kudrawiec, *Semiconductor Science and Technology* **30**, 094001 (2015).

63. M. P. Polak, P. Scharoch, R. Kudrawiec, *Journal of Physics D: Applied Physics* **50**, 195103 (2017).

64. M. P. Polak, P. Scharoch, R. Kudrawiec, *Journal of Physics D: Applied Physics* **50**, 195103 (2017).

65. W. Porod, D. K. Ferry, *Phys. Rev. B* **27**, 2587–2589 (4 1983).

66. J. Pulikkotil, A. Chroneos, *Journal of Applied Physics* **110** (2011).

67. Z. Qi, H. Sun, M. Luo, Y. Jung, D. Nam, *Journal of Physics: Condensed Matter* **30**, 334004 (2018).

68. N. J. Ramer, A. M. Rappe, *Phys. Rev. B* **62**, R743–R746 (2 2000).

69. S. Richard, F. Aniel, G. Fishman, *Phys. Rev. B* **72**, 245316 (24 2005).

70. D. Rideau, M. Feraille, L. Ciampolini, M. Minondo, C. Tavernier, H. Jaouen, A. Ghetti, *Phys. Rev. B* **74**, 195208 (19 2006).

71. C. Rödl, T. Sander, F. Bechstedt, J. Vidal, P. Olsson, S. Laribi, J.-F. Guillemoles, *Phys. Rev. B* **92**, 045207 (4 2015).

72. O. Rubel, A. Bokhanchuk, S. J. Ahmed, E. Assmann, *Physical Review B* **90** (2014).

73. M. Sahnoun, R. Khenata, H. Baltache, M. Rérat, M. Driz, B. Bouhafs, B. Abbar, *Physica B: Condensed Matter* **355**, 392–400 (2005).

74. A. M. Saitta, S. de Gironcoli, S. Baroni, *Phys. Rev. Lett.* **80**, 4939–4942 (22 1998).

75. D. Saladukha, M. Clavel, F. Murphy-Armando, G. Greene-Diniz, M. Grüning, M. Hudait, T. Ochalski, *Physical Review B* **97** (2018).

76. J. R. Sánchez-Pérez, C. Boztug, F. Chen, F. F. Sudradjat, D. M. Paskiewicz, R. Jacobson, M. G. Lagally, R. Paiella, *Proceedings of the National Academy of Sciences* **108**, 18893–18898, eprint: `https://www.pnas.org/content/108/47/18893.full.pdf` (2011).

77. I. Saunders, J. Nutting, *Metal Science* **18**, 571–576, eprint: `https://doi.org/10.1179/030634584790419629` (1984).

78. P. Scharoch, N. Janik, M. Wiśniewski, H. S. Mączko, M. Gładysiewicz, M. P. Polak, R. Kudrawiec, *Computational Materials Science* **187**, 110052 (2021).

79. P. Scharoch, M. Winiarski, M. Polak, *Computational Materials Science* **81** (2014).

80. J. Shen, J. Zi, X. Xie, P. Jiang, *Phys. Rev. B* **56**, 12084–12087 (19 1997).

81. R. A. Soref, C. H. Perry, *Journal of Applied Physics* **69**, 539–541, eprint: `https://doi.org/10.1063/1.347704` (1991).

82. W. Sun, C.-K. Tan, J. J. Wierer, N. Tansu, *Scientific Reports* **8**, 3109 (2018).

83. X. Sun, J. Liu, L. C. Kimerling, J. Michel, *IEEE Journal of Selected Topics in Quantum Electronics* **16**, 124–131 (2010).

84. M. Torrent, F. Jollet, F. Bottin, G. Zérah, X. Gonze, *Computational Materials Science* **42**, 337–351 (2008).

85. F. Tran, P. Blaha, *Phys. Rev. Lett.* **102**, 226401 (22 2009).

86. F. Tran, P. Blaha, *Physical review letters* **102**, 226401 (2009).

87. H. Tran, C. G. Littlejohns, D. J. Thomson, T. Pham, A. Ghetmiri, A. Mosleh, J. Margetis, J. Tolle, G. Z. Mashanovich, W. Du, B. Li, M. Mortazavi, S.-Q. Yu, *Frontiers in Materials* **6**, 278 (2019).

88. `https://web.mit.edu/course/3/3.11/www/modules/trans.pdf`, Accessed: 2021-04-09.

89. C. G. Van de Walle, *Phys. Rev. B* **39**, 1871–1883 (3 1989).

90. C. S. Wang, B. M. Klein, *Phys. Rev. B* **24**, 3393–3416 (6 1981).

91. W. Wegscheider, K. Eberl, U. Menczigar, G. Abstreiter, *Applied Physics Letters* **57**, 875–877, eprint: `https://doi.org/10.1063/1.104264` (1990).

92. S.-H. Wei, A. Zunger, *Applied Physics Letters* **72**, 2011–2013 (1998).

93. B. Welber, M. Cardona, Y.-F. Tsay, B. Bendow, *Phys. Rev. B* **15**, 875–879 (2 1977).

94. W.-J. Yin, X.-G. Gong, S.-H. Wei, *Phys. Rev. B* **78**, 161203 (16 2008).

95. S. Zaima, O. Nakatsuka, N. Taoka, M. Kurosawa, W. Takeuchi, M. Sakashita, *Science and Technology of Advanced Materials* **16**, 043502 (2015).

96. K. Zelazna, M. P. Polak, P. Scharoch, J. Serafinczuk, M. Gladysiewicz, J. Misiewicz, J. Dekoster, R. Kudrawiec, *Applied Physics Letters* **106**, 142102, eprint: `https://doi.org/10.1063/1.4917236` (2015).

97. X. Zhang, C. Ying, S. Quan, G. Shi, Z. Li, *Computational Materials Science* **58**, 12–16 (2012).

98. Y. Zhang, Z. Iqbal, S. Vijayalakshmi, S. Qadri, H. Grebel, *Solid State Communications* **115**, 657–660 (2000).

99. C.-Z. Zhao, S.-Y. Sun, M.-M. Zhu, Y. Guo, *Applied Physics A*, 126:131 (2020).

100. Z. Zhu, J. Xiao, H. Sun, Y. Hu, R. Cao, Y. Wang, L. Zhao, J. Zhuang, *Phys. Chem. Chem. Phys.* **17**, 21605–21610 (33 2015).

101. A. Zunger, S.-H. Wei, L. G. Ferreira, J. E. Bernard, *Phys. Rev. Lett.* **65**, 353–356 (3 1990).

Appendix A

Chosen proofs and derivations

In this chapter will be presented chosen proofs and derivations used it certain parts of the thesis above.

Elastic constants derivation

This derivation shows the path of transformations done to achieve elastic constants. In general case, during change of Cartesian system, all of the matrix components play it's role in transformation. As it is shown in here [88]. Each tensor row represent different cube wall, while each column sets the direction of strain/stress (Fig. A.1).

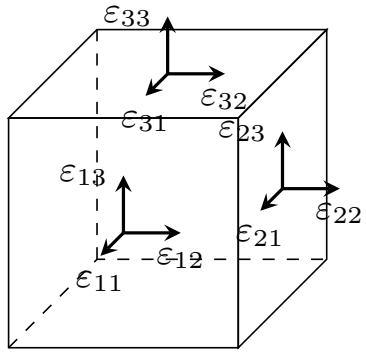

Figure A.1: Interpretation of strain/stress tensor elements.

In the equations below, such notation is used, that strain and stress tensors are represented by vectors made of independent tensor elements:

$$\begin{bmatrix} \varepsilon_{11} & \varepsilon_{12} & \varepsilon_{13} \\ \varepsilon_{21} & \varepsilon_{22} & \varepsilon_{23} \\ \varepsilon_{31} & \varepsilon_{32} & \varepsilon_{33} \end{bmatrix} \Rightarrow \begin{bmatrix} \varepsilon_1(\varepsilon_{11}) \\ \varepsilon_2(\varepsilon_{22}) \\ \varepsilon_3(\varepsilon_{33}) \\ \varepsilon_4(\varepsilon_{23} = \varepsilon_{32}) \\ \varepsilon_5(\varepsilon_{13} = \varepsilon_{31}) \\ \varepsilon_6(\varepsilon_{12} = \varepsilon_{21}) \end{bmatrix}. \tag{A.1}$$

Such a conversion may be used, due to symmetry of strain/stress tensor, independently of space group, which is also visible on Fig. A.1. This symmetry will occur even in the case of unorthogonal lattice vectors.

All the desired elastic properties, in this part of work, are for pure group IV materials, which crystallize in diamond structure (#227). The symmetry also affects the stress tensor equation which, for diamond structure, is as follows:

$$\begin{bmatrix}\sigma_1\\ \sigma_2\\ \sigma_3\\ \sigma_4\\ \sigma_5\\ \sigma_6\end{bmatrix} = \begin{bmatrix}c_{11} & c_{12} & c_{12} & 0 & 0 & 0\\ c_{12} & c_{11} & c_{12} & 0 & 0 & 0\\ c_{12} & c_{12} & c_{11} & 0 & 0 & 0\\ 0 & 0 & 0 & c_{44} & 0 & 0\\ 0 & 0 & 0 & 0 & c_{44} & 0\\ 0 & 0 & 0 & 0 & 0 & 0c_{44}\end{bmatrix} \begin{bmatrix}\varepsilon_1\\ \varepsilon_2\\ \varepsilon_3\\ \varepsilon_4\\ \varepsilon_5\\ \varepsilon_6\end{bmatrix}. \tag{A.2}$$

For that specific space group, elastic tensor has only three non-zero independent elements: c_{11}, c_{12} and c_{44}.

The matrix equation A.2 can be simply written as:

$$\sigma_i = \sum_j c_{ij}\varepsilon_j \tag{A.3}$$

Space group symmetry slightly simplifies the system of equations, from which will be chosen ones to derive elastic constants, to four:

$$\begin{cases}\sigma_1 = c_{11}\varepsilon_1 + c_{12}\varepsilon_2 + c_{12}\varepsilon_3\\ \sigma_2 = c_{12}\varepsilon_1 + c_{11}\varepsilon_2 + c_{12}\varepsilon_3\\ \sigma_3 = c_{12}\varepsilon_1 + c_{12}\varepsilon_2 + c_{11}\varepsilon_3\\ \sigma_4 = c_{44}\varepsilon_4.\end{cases} \tag{A.4}$$

From first equation of Eq. A.4 c_{11} is derived:

$$\begin{aligned}\sigma_1 - c_{12}(\varepsilon_2 + \varepsilon_3) &= c_{11}\varepsilon_1\\ c_{11} &= \frac{\sigma_1 - c_{12}(\varepsilon_2 + \varepsilon_3)}{\varepsilon_1}\end{aligned} \tag{A.5}$$

and from second equation c_{12}:

$$\begin{aligned}\sigma_2 &= c_{12}(\varepsilon_1 + \varepsilon_3) + \varepsilon_2\frac{\sigma_1 - c_{12}(\varepsilon_2 + \varepsilon_3)}{\varepsilon_1}\\ c_{12}(\varepsilon_1 + \varepsilon_3) - c_{12}\frac{(\varepsilon_2 + \varepsilon_3)\varepsilon_2}{\varepsilon_1} &= \sigma_2 - \sigma_1\frac{\varepsilon_2}{\varepsilon_1}\\ c_{12}(\varepsilon_1 + \varepsilon_2 - \frac{(\varepsilon_2 + \varepsilon_3)\varepsilon_2}{\varepsilon_1}) &= \sigma_2 - \sigma_1\frac{\varepsilon_2}{\varepsilon_1}\end{aligned} \tag{A.6}$$

The equations above (Eq. A.5, A.6) along with fourth equation from Eq. A.4 gives general solution for diamond structure elastic constants in form:

$$\begin{cases} c_{11} = \frac{\sigma_1}{\varepsilon_1} - \frac{(\sigma_2 - \sigma_1 \frac{\varepsilon_2}{\varepsilon_1})(\varepsilon_2 + \varepsilon_3)}{\varepsilon_1(\varepsilon_1 + \varepsilon_2) - \varepsilon_2(\varepsilon_2 + \varepsilon_3)} \\ c_{12} = \frac{\sigma_2 - \sigma_1 \frac{\varepsilon_2}{\varepsilon_1}}{\varepsilon_1 + \varepsilon_2 - \frac{\varepsilon_2(\varepsilon_2 + \varepsilon_3)}{\varepsilon_1}} \\ c_{44} = \frac{\sigma_4}{\varepsilon_4} \end{cases} \tag{A.7}$$

Due to technical limitations of relaxation algorithms implemented in ABINIT code, at least one lattice vector had to be orthogonal to the other vectors. Supercells used in relaxation process are presented on figs. 2.2 and 2.3. Strains could be applied only in lattice vectors directions. Therefore, the results obtained in relaxation process do not include shear strain and stress.

To solve the equations A.7 there must be chosen certain systems, from which data (stress / strain) will be taken. For calculation of c_{11} and c_{12} [100] straining direction will be the most suitable, due to fact, that $\sigma_1 = \sigma_2$, $\varepsilon_1 = \varepsilon_2$ and $\sigma_4 = \sigma_5 = \sigma_6 = \varepsilon_4 = \varepsilon_5 = \varepsilon_6 = 0$.

To calculate c_{44}, shear strain must be inducted. Therefore, [110] or [111] straining direction must be used here. Due to less complicated system, [110] direction was chosen for further analysis. The c_{44} elastic constant is described as:

$$c_{44} = \frac{\sigma_4}{\varepsilon_4} = \frac{\sigma_5}{\varepsilon_5} = \frac{\sigma_6}{\varepsilon_6}. \tag{A.8}$$

In general, ε can be described by tangent of an angle in strained system. For [110] direction, in plane lattice constants (a_1 and a_2) has different value due to shear strain, which leads to ε_6 in form:

$$\varepsilon_6 = tan\Delta\vartheta = tan(\pi/4 - atan(\frac{a_2}{a_1})). \tag{A.9}$$

Unfortunately, $\sigma_6 = 0$ in this case as well (definition of supercell required it), but it can be taken directly from here[88] in form:

$$\sigma_6 = (\sigma_2 - \sigma_1) sin\Delta\vartheta cos\Delta\vartheta. \tag{A.10}$$

where ϑ is an angle of triangle made by supercell lattice vectors a_1 and a_2 (which are orthogonal).

After a few trivial algebraic transformations, the final equations for calculating elastic constants are as follow:

$$\begin{cases} c_{11} = \frac{\sigma_1}{\varepsilon_1} - \frac{\varepsilon_1 + \varepsilon_3}{\varepsilon_1} \frac{\sigma_3\varepsilon_1 - \sigma_1\varepsilon_3}{2\varepsilon_1^2 - \varepsilon_3(\varepsilon_1 + \varepsilon_3)} \\ c_{12} = \frac{\sigma_3\varepsilon_1 - \sigma_1\varepsilon_3}{2\varepsilon_1^2 - \varepsilon_3(\varepsilon_1 + \varepsilon_3)} \\ c_{44} = (\sigma_2 - \sigma_1) sin^2\Delta\vartheta \end{cases} \tag{A.11}$$

It should be noted that elastic constants, as all of the associated theory, work in linear regime, which is not apparent in higher strains. In fact, even in the case of 1% of deformation, non-linearity is noticeable enough to give slightly different results in compressive and tensile strains. Therefore, results given in chapter 2 are arithmetic average of both types of strain.

Supercell to primitive cell transformation

The primitive cell of diamond structure can be defined through transformation matrix from conventional cell as

$$\begin{bmatrix} a_1' \\ a_2' \\ a_3' \end{bmatrix} = \begin{bmatrix} 0 & 0.5 & 0.5 \\ 0.5 & 0 & 0.5 \\ 0.5 & 0.5 & 0 \end{bmatrix} \begin{bmatrix} a_1 \\ a_2 \\ a_3 \end{bmatrix}, \tag{A.12}$$

while transformation from [100] and [110] strain direction supercell as

$$\begin{bmatrix} a_1' \\ a_2' \\ a_3' \end{bmatrix} = \begin{bmatrix} 0.5 & 0.5 & 0 \\ -0.5 & 0.5 & 0 \\ 0 & 0 & 1 \end{bmatrix} \begin{bmatrix} a_1 \\ a_2 \\ a_3 \end{bmatrix}, \tag{A.13}$$

and for [111] as

$$\begin{bmatrix} a_1' \\ a_2' \\ a_3' \end{bmatrix} = \begin{bmatrix} 0.5 & 0 & 0.5 \\ -0.5 & -0.5 & 0 \\ -1 & 1 & 1 \end{bmatrix} \begin{bmatrix} a_1 \\ a_2 \\ a_3 \end{bmatrix}. \tag{A.14}$$

Converting the supercell to primitive cell requires transformation matrix. Not only to follow changes in lattice vectors but also the vectors defining atomic positions in unit cell. Due to chosen relaxation algorithm they can vary as well. In case of equilibrium systems the transformation is rather obvious but it can be useful as testing object. Of higher importance are distorted structures. To avoid problems with numerical representation of long decimal numbers, which occur concerning little deformations, as an outcome only length and angles between lattice vectors are given, instead of Cartesian representation.

Matrix multiplication is not commutative, thus there is a need to find inversions of supercell matrices. As a result matrix from supercells to conventional cells are given below. For [100] and [110] strain directions

$$\begin{bmatrix} a_1' \\ a_2' \\ a_3' \end{bmatrix} = \begin{bmatrix} 1 & -1 & 0 \\ 1 & 1 & 0 \\ 0 & 0 & 1 \end{bmatrix} \begin{bmatrix} a_1 \\ a_2 \\ a_3 \end{bmatrix}, \tag{A.15}$$

and for [111] direction

$$\begin{bmatrix} a_1' \\ a_2' \\ a_3' \end{bmatrix} = \begin{bmatrix} 2/3 & -2/3 & -1/3 \\ -2/3 & -4/3 & 1/3 \\ 4/3 & 2/3 & 1/3 \end{bmatrix} \begin{bmatrix} a_1 \\ a_2 \\ a_3 \end{bmatrix}. \tag{A.16}$$

With inversions given, the final transformations can be built. Multiplication from conventional cell to primitive cell times supercell to conventional cell, in that exact order, gives required matrix transformations. From [100] and [110] strain directions to primitive cell

$$\begin{bmatrix} a_1' \\ a_2' \\ a_3' \end{bmatrix} = \begin{bmatrix} -0.25 & 0.25 & 0.5 \\ 0.25 & 0.25 & 0.5 \\ 0 & 0.5 & 0 \end{bmatrix} \begin{bmatrix} a_1 \\ a_2 \\ a_3 \end{bmatrix}, \tag{A.17}$$

and for [111] direction

$$\begin{bmatrix} a_1' \\ a_2' \\ a_3' \end{bmatrix} = \begin{bmatrix} -0.75 & 0.25 & 0.5 \\ -0.25 & 0.5 & 0.75 \\ 0 & -0.25 & 0.25 \end{bmatrix} \begin{bmatrix} a_1 \\ a_2 \\ a_3 \end{bmatrix}. \tag{A.18}$$

List of acromins

ab initio	a Latin term meaning "from the beginning", in scientific context means "from first principles". 4, 12, 27, 35–37, 39, 45, 51, 55, , 79
AM	Alchemical Mixing. 37–40,
ansatz	an educated guess or an additional assumption made to help solve a problem, and which is later verified to be part of the solution by its results.
BZ	first Brillouin Zone. x, xi, 6, 10, 14, 16, 28, 36–40, 46, 55–57, , 79
CB	conduction band. 10, 18, 19, 28, 39,
CH	crystal–field split–off holes. 47,
conventional cell	conventional cell is the smallest unit cell that contains the same point group symmetries as the overall lattice. 72,
CPA	coherent potential approximation. 37,
DFT	Density Functional Theory. ix, 3–6, 20, 28, 32, 34–36, 39–41,
DOS	density of states. 57,
EOS	equation of state. 32,
GGA	Generalized Gradient Approximation. 4,
HGH	Hartwigsen-Goedecker-Hutter pseudopotential. 11, 33, 38, 39,
HH	heavy holes. x, xi, 18–20, 23, 26, 28, 47,
HMA	highly mismatched alloys. 37, 38,
KKR	Korringa–Kohn–Rostoker method. 37,
LDA	Local Density Approximation. ix, 3, 10, 14, 20, 39, 57,
LDOS	local density of states.
LH	light holes. x, xi, 18–20, 23, 26, 28, 47,
mBJLDA	modified Becke–Johnson Local Density Approximation. x, 11, 20, 33, 39, 46, 57,
PAW	Projector Augmented Wave method. 5, 10, 11, 13, 32, 34, 39, 46, 57,

LIST OF ACROMINS

PBE	Perdew, Burke, Ernzerhof functional.
primitive cell	smallest unit cell that contain only one lattice point. 38, 40, 72,
SC	self–consistent. 39,
SO	spin–orbit interaction. 19, 20, 46, 47,
SQS	Special Qausirandom Structures. 35, 36, 55,
TB	tight-binding. 27,
VB	valence band. 10, 18, 28, 34,
VBM	valence band maximum. 12, 19,
VCA	virtual crystal approximation. 37,
XC	exchange–correlation. 3, 4, 11, 33, 57,

List of symbols

ε_{ind} constrained change of length relative to equilibrium length.
ε_{opt} change of length in relaxed direction relative to equilibrium length.

ν Poisson's ratio.

σ stress induced by straining material.

E_{tot} Total energy of system.

List of URL

VESTA – visualization program	http://www.jp-minerals.org/vesta/en/
ABINIT – *ab initio* program	https://www.abinit.org/
VASP – *ab initio* program	https://www.vasp.at/
Bilbao – online crystallographic server	https://www.cryst.ehu.es/
WCNS – Wrocław Centre of Networking and Supercomputing	https://www.wcss.pl/en/
SeeK-path – online tool for BZ visualization	
https://www.materialscloud.org/work/tools/seekpath	
Cyfronet AGH – Academic Computer Centre Cyfronet AGH	
https://www.cyfronet.krakow.pl/en/4421,main.html	